Hindawi
Structural Control and Health Monitoring
Volume 2023, Article ID 1150525, 22 pages
https://doi.org/10.1155/2023/1150525

Research Article

Asymmetric and Cubic Nonlinear Energy Sink Inerters for Mitigating Wind-Induced Responses of High-Rise Buildings

Qinhua Wang,[1] **Huaxiao Wu**,[2] **Haoshuai Qiao**,[3] **Xianfeng Yu**,[4] **and Peng Huang**[3]

[1]*School of Civil Engineering and Architecture, Southwest University of Science and Technology, Mianyang 621010, China*
[2]*Tsinghua Shenzhen International Graduate School, Tsinghua University, Shenzhen 518055, China*
[3]*State Key Laboratory of Disaster Reduction in Civil Engineering, Tongji University, Shanghai 200092, China*
[4]*State Key Laboratory of Subtropical Building Science, South China University of Technology, Guangzhou 510640, China*

Correspondence should be addressed to Haoshuai Qiao; haoshuai_qiao@tongji.edu.cn

Received 16 June 2023; Revised 31 August 2023; Accepted 19 September 2023; Published 11 October 2023

Academic Editor: Yoshiki Ikeda

Flexible high-rise buildings with low damping are prone to excessive vibration under strong wind loads. To explore a light-weight control device having desirable mitigation effects on responses and sound robustness against deviations in tuning parameters, the performance of two novel inerter-integrated nonlinear energy sinks (NESIs), i.e., asymmetric nonlinear energy sink inerter (Asym NESI) and cubic NESI, on wind-induced vibration control of super high-rise buildings is assessed in the present work. Based on the wind loads obtained from wind tunnel tests, a super high-rise building with a 300 m height is taken as the host structure in the numerical case study. The results show that Asym NESI can achieve reduction ratios of 38.5% and 11.3% on extreme acceleration and displacement, respectively, while the sensitivity indices of Asym NESI on displacement and acceleration control are only 70.5% and 62.5% of those of tuned mass damper inerter (TMDI) having identical mitigation effects. Although the sensitivity indices of cubic NESI are only 5.5% and 29.8% of those of TMDI, the moderate mitigation effects and large nonlinear stiffness ratio may prohibit its practical implementation. Overall, Asym NESI could be an alternative to TMDI due to the same mitigation effects but better robustness against possible detuning.

1. Introduction

Vibration control of flexible high-rise buildings subjected to wind loads has attracted the attention of researchers for decades [1]. Especially for high-rise buildings with aspect ratios over 3, the across-wind responses usually exceed along-wind responses due to vortex shedding effects [2], and vibration control strategies are required to satisfy survivability and serviceability criteria.

To mitigate wind-induced vibration, employing passive vibration control devices is one of the widely-adopted strategies attributed to the independence of supplemental energy, low cost, easy implementation, and so on [3, 4]. Among the passive devices, tuned mass damper (TMD) has drawn extensive attention due to its simplicity and effectiveness and has been implemented in a great number of real-life buildings [5]. However, the trend of increasing height of newly constructed high-rise buildings implies a rapidly increasing weight of the structure, in which case a significantly heavy attached mass of conventional TMD is demanded to fulfill desirable control performance [6]. To alleviate the demand of massive physical masses of control devices, a novel inertia element termed inerter [7] was integrated to conventional control devices, and a series of linear inerter-based vibration absorbers (IVAs) emerged thereafter [3], e.g., tuned inerter damper [8, 9], TMDI [10, 11], multiple tuned mass damper inerters [12, 13], tuned liquid column damper inerter [14, 15], tuned tandem mass dampers inerters [16, 17], tandem tuned mass damper inerter [18], and inerter-connected double tuned mass damper [19]. Benefitting from the considerable mass amplification effect, i.e., the apparent mass of an inerter can be thousands of times its physical mass [20], IVAs were commonly reported to outperform their conventional

competitors on both response reduction and robustness [14, 21, 22]. Among various IVAs, TMDI is one of the most studied IVAs due to its direct relation with traditional TMD. Giaralis and Petrini [23] numerically investigated the control performance of TMDI on the displacement and acceleration responses of a 76-story building under across-wind loads simulated by an empirical spectrum [2]. The multistory spanning TMDI was found to outperform TMD in terms of better mitigation effects and significantly smaller strokes. Based on the wind loads obtained from wind tunnel tests, Wang et al. [24, 25] further evaluated the mitigation effects of TMDI on wind-induced vibration of a tall building at 24 wind directions. Considering the practicality of the physical mass of an inerter, a tuned inerter damper (TID) was reported to outperform TMDI and TMD having the same device mass under the assumption that the inertance of an inerter is 200 times its physical mass. Besides investigating the performance, the strategies of parametric design for IVAs were also developed. Based on a simplified single-degree-of-freedom (SDOF) model, Su et al. [26] derived the closed-form tuning formulae of TMDI considering an arbitrary installation layout of TMDI via a filter-based approach. Kaveh et al. [27] adopted a meta-heuristic optimization algorithm, i.e., colliding bodies optimization (CBO) algorithm, to find the optimal parameters of TMDI for controlling a 10-story benchmark building. Further, Kaveh et al. [28] compared the parameters and control performance of TMDI optimized based on the simplified SDOF model and multi-degree-of-freedom (MDOF) model, pursuing a maximum reduction on the H_∞ norm of the roof displacement transfer function. The results showed that the MDOF model is recommended to be employed for TMDI design, while the SDOF model should be adopted with caution. Since modal coupling effects were neglected in the process of establishing the simplified SDOF model, Qiao et al. [29] adopted the Sherman–Morrison matrix inversion operation to derive the explicit forms of entries in the matrix of frequency response functions of the controlled structure based on the MDOF model and, correspondingly, proposed a new parametric design strategy.

Although the robustness of linear IVAs was commonly reported to be better than their conventional counterparts, the linear nature of IVA implies the inherent deficiency of detuning; that is, the desirable control performance of IVAs still relies on a proper tuning [26], and thus IVAs are sensitive to the deviations in tuning parameters. It is noted that the additional aerodynamic damping and aerodynamic stiffness of high-rise buildings under strong wind loads could alter the dynamic behaviors of the primary structure. Hence, passive IVAs probably encounter detuning issues during their service life. In this regard, it is important to seek control devices having competitive control performance to IVAs with more sound robustness.

In comparison to linear control devices, whose mitigation effects are mainly attributed to the resonant oscillation around the to-be-controlled vibration mode of the primary structure, the nonlinear nature of nonlinear energy sink (NES) endows them with the capability to resonate and irreversibly absorb energy from multiple vibration modes [30, 31] and thus generally exhibits attractive vibration mitigation effects but better robustness than linear absorbers like TMD [32]. With the ongoing proposals of IVAs, researchers started to introduce inerter to NES to alleviate the requirement of a heavy attached mass and enhance the control performance of traditional NESs. Zhang et al. [33] arranged an inerter to a cubic-type stiffness element and a dashpot element of NES in a parallel layout and proposed NESI. Under ground motion excitations, the better control performance of NESI than NES was validated in terms of amplitude-frequency response and energy absorption. Zhang et al. [34] proposed another NESI by replacing the attached mass of NES with a grounded inerter. Since this NESI behaved like an NES having an attached mass of b (inertance of the inerter) and b was usually designed to be much larger than the attached mass of traditional NES, the grounded NESI showed better vibration suppression performance under ground motion excitations than NES. In the same year, the grounded NESI was also independently proposed by Javidialesaadi et al. [35]. Besides the better control performance of NESI than NES, the incorporation of a grounded inerter showed a greater enhancement in the control performance of NES than that of TMD. However, all NESIs above were developed by introducing an inerter to cubic-type NES, and its drawback was still inherited in the novel cubic NESI; that is, satisfactory performance was only achieved at a suitable level of input energy. To address this deficiency, Wang et al. [36] connected the attached mass of an asymmetric NES and an arbitrary DOF of the structure with an inerter and named the device after Asym NESI. In a numerical case of a three-story steel-frame structure subjected to seismic loads, the robustness of Asym NESI was found to be better than TMDI and cubic NESI against changing frequencies of the host structure and was less sensitive to variations in initial velocity than cubic NESI. Further, Wang et al. [37] updated the equations of motion for Asym NESI by integrating the damping embedded in the inerter part and validating it through experiments. The updated model was used to investigate the control performance of Asym NESI in the seismic design of a three-story steel-frame structure, wherein Asym NESI exhibited similar control performance as TMDI and strong robustness against variations in structural property and energy level.

The vibration mitigation effects of both Asym and cubic NESIs were only studied under ground motion excitations, while to the best of the authors' knowledge, no investigations on the parametric optimization and performance assessment of NESIs for wind-induced vibration control have been conducted so far. To address this gap, the present work investigates and compares the mitigation effects and robustness of both Asym NESI and cubic NESI with those of TMDI for wind-induced vibration control. Having formulated the equations of motions of the NESI-controlled MDOF structure based on a planar lumped mass model, the performance indices regarding mitigation effects and robustness are introduced. Based on a real case of a tall building along with wind loads obtained from wind tunnel tests, the optimal parameters of Asym NESI, cubic NESI, and

TMDI are numerically obtained and discussed. The control performance of the optimum representatives of the three devices is further scrutinized. After evaluating the robustness of control performance against deviations in tuning parameters, practical considerations concerning the realization of nonlinear springs and the initial cost of the devices are discussed.

2. Mathematical Model of Asym NESI-Controlled High-Rise Buildings Subjected to Wind Loads

The translational motion of a high-rise building is described by a planar lumped mass model as shown in Figure 1(a), which is broadly adopted in the performance analyses of control devices for the wind-resistant design of high-rise buildings [17, 23, 38] due to its low computational cost and ease of reproducibility. Since some important issues, e.g., axial deformation and nonlinear geometry, are not considered in the simplified mode, further analyses based on the finite element model are still required before the implementation of full-scale control devices. An Asym NESI is installed on the j^{th} floor ($j = 1, \ldots, n$, n is the total number of floors) and connected to the i^{th} floor ($i = 1,\ldots,n$) by an ideal inerter having an inertance of b (unit: kg). The attached mass weighting m_{Asym} is connected to the j^{th} floor by a nonlinear spring having a stiffness coefficient of k_{nl}, a linear spring having a stiffness coefficient of k_l, and a dashpot element having a damping coefficient of c_l. In comparison to cubic NESI in Figure 1(b), the nonlinear spring of Asym NESI is prestretched by a set distance r to generate an asymmetric restoring force, and the linear spring is used to keep the mass statically balanced.

Particularly, the realization of nonlinear spring is detailedly introduced to underpin the feasibility of NESIs. One of the most commonly adopted realization approaches of nonlinear spring is arranging a pair of linear springs in serial, in which way the nonlinear restoring force is generated due to the geometric nonlinearity. As illustrated in Figure 2(a), the nonlinear restoring force F_{Rnl} is provided by two linear springs having stiffness coefficients of k and unstretched lengths of L.

When the joint moves away from its balance point at displacement x, F_{Rnl} can be explicitly expressed as

$$F_{Rnl} = 2kx\left(1 - \frac{L}{\sqrt{L^2 + x^2}}\right). \tag{1}$$

By Taylor-expanding the fraction term in equation (1) about $x = 0$, we obtain

$$\begin{aligned} F_{Rnl} &= 2kx\left[1 - 1 + \frac{x^2}{2L^2} + O\left(x^4\right)\right] \\ &= \frac{k}{L^2}x^3 + O\left(x^5\right). \end{aligned} \tag{2}$$

Thus, the two linear springs behave like a nonlinear spring having a nonlinear stiffness of k_{nl} in Figure 1(b) when $O(x^5)$ is neglected, as expressed in the following equation:

$$\begin{aligned} F_{Rnl} &= \frac{k}{L^2}x^3 \\ &= k_{nl}x^3. \end{aligned} \tag{3}$$

Further, when the joint is pulled to a distance of r from its original balance location using a linear spring having a stiffness coefficient of k_l, the spring system of Asym NESI is obtained, as shown in Figure 2(b). In this system, r can be flexibly adjusted to the design value by changing the deformation length of the linear spring, i.e., x_l, as expressed in the following equation:

$$r = \sqrt[3]{\frac{k_l x_l}{k_{nl}}}. \tag{4}$$

Two photographs of cubic NES and Asym NES (without inerter) are presented in Figure 3 to illustrate the spring systems.

Besides NESIs, TMDI is also presented in Figure 1 as it is set as a competitor to two NESIs in the present work. Particularly, Asym NESI can be regarded as a general form of TMDI and cubic NESI, since TMDI and cubic NESI can be retrieved by setting $k_{nl} = r = 0$ and $k_l = r = 0$, respectively. In this regard, only the equations of motion of the Asym NESI-equipped structure are introduced hereafter.

The total restoring force of Asym NESI on the j^{th} floor can be expressed as

$$F_A(t) = k_{nl}\left[x_{\text{Asym}}(t) + r\right]^3 + k_l x_{\text{Asym}}(t) + f_s, \tag{5}$$

where x_{Asym} is the displacement of the attached mass relative to the j^{th} story. $f_s = -k_{nl}r^3$ is the initial force in the nonlinear spring when x_{Asym} is equal to zero. By substituting f_s into equation (5), the total restoring force can be rewritten as

$$F_A(t) = k_{nl}x(t)^3_{\text{Asym}} + 3k_{nl}rx(t)^2_{\text{Asym}} + \left(3k_{nl}r^2 + k_l\right)x_{\text{Asym}}(t). \tag{6}$$

Thus, the equations of motion of high-rise buildings controlled by Asym NESI under wind loads can be expressed as

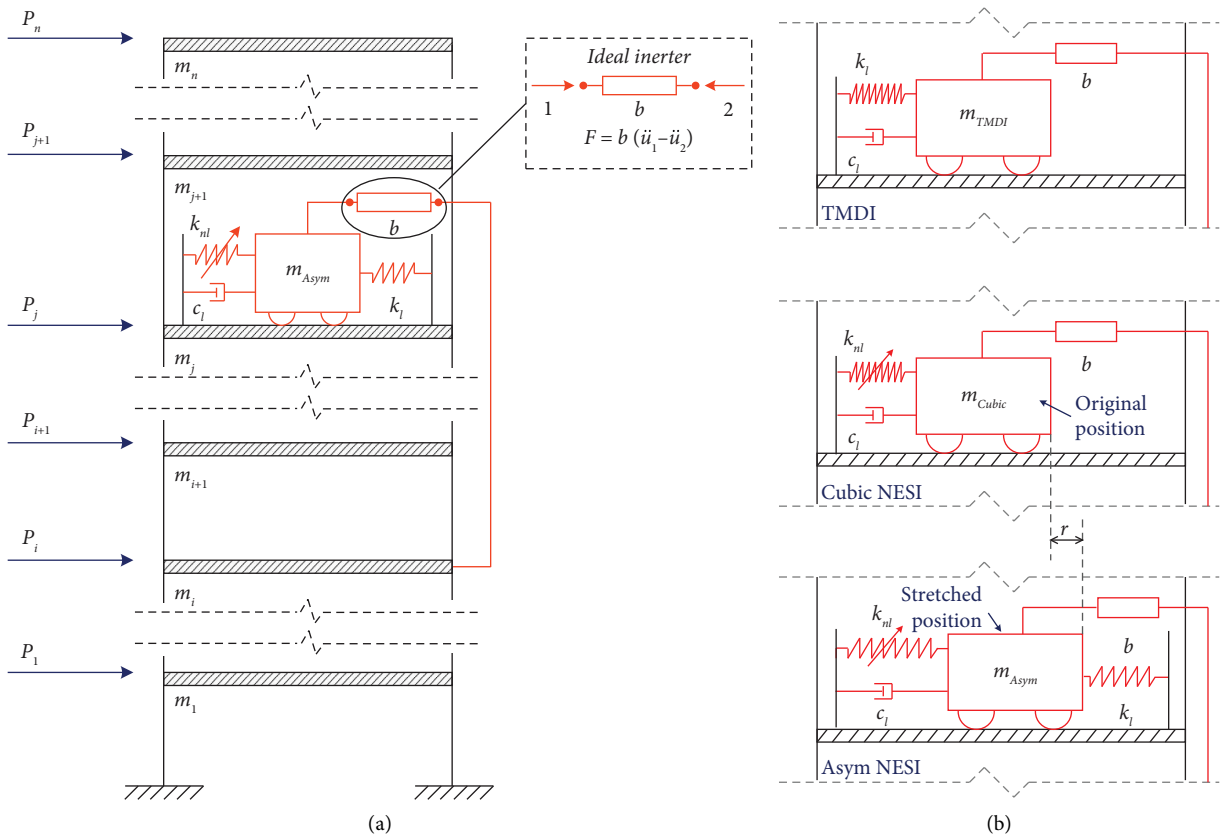

FIGURE 1: (a) Lumped mass model of a high-rise building controlled by an Asym NESI; (b) mechanical layouts of TMDI, cubic NESI, and Asym NESI.

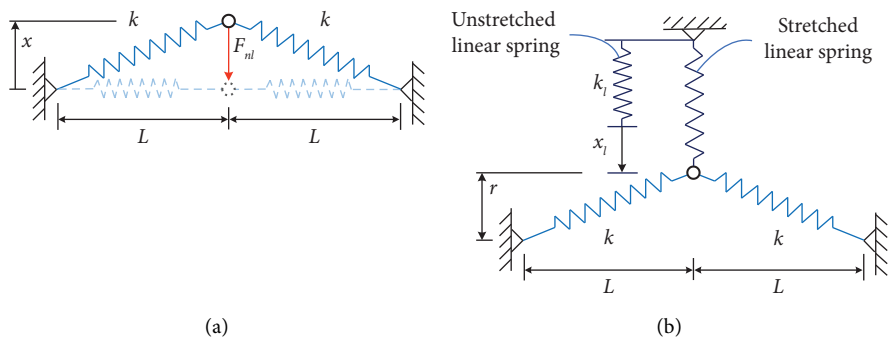

FIGURE 2: Spring systems in (a) cubic NESI and (b) Asym NESI.

$$[M]\left\{\ddot{x}\,(t)\ddot{x}_{\mathrm{Asym}}(t)\right\}+[C]\begin{Bmatrix}\dot{x}(t)\\ \dot{x}_{\mathrm{Asym}}(t)\end{Bmatrix}+[K(t)]\begin{Bmatrix}x(t)\\ x_{\mathrm{Asym}}(t)\end{Bmatrix}=\begin{Bmatrix}p(t)\\ 0\end{Bmatrix}, \tag{7}$$

where $\{\ddot{x}(t)\}$, $\{\dot{x}(t)\}$, and $\{x(t)\}$ are n-by-1 vectors of acceleration, velocity, and displacement of DOFs of the primary building at an arbitrary time t, respectively, and are related to the ground. $\ddot{x}_{\mathrm{Asym}}(t)$, $\dot{x}_{\mathrm{Asym}}(t)$, and $x_{\mathrm{Asym}}(t)$ are corresponding responses of the attached mass of Asym NESI related to the installation floor. $\{p(t)\}$ denotes the vector of the aerodynamic forces applied on each floor. Asym NESI is assumed to be installed inside the building and not exposed to wind loads. $[M]$, $[C]$, and $[K(t)]$ are $(n+1)$-by-$(n+1)$ mass, damping, and stiffness matrices of the controlled structure, respectively, and can be expanded as

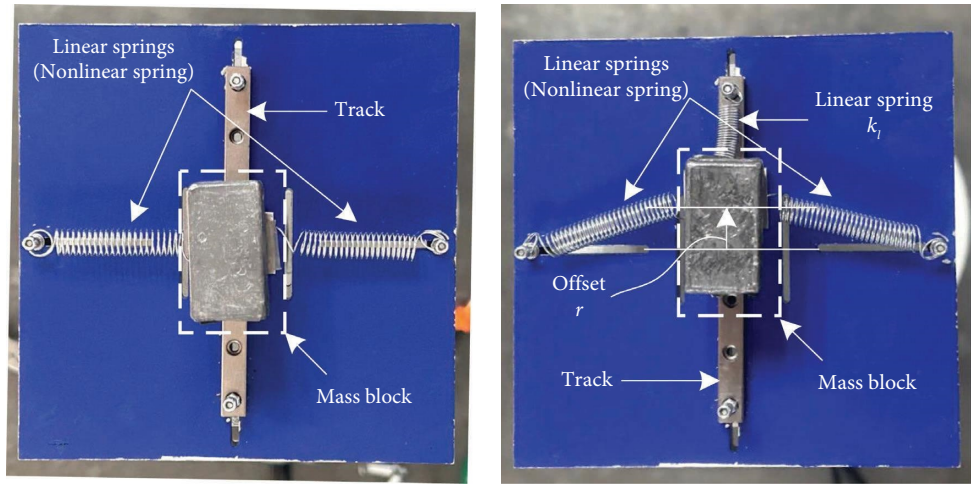

(a) (b)

Figure 3: Top views of (a) cubic NES and (b) Asym NES.

$$
\begin{aligned}
[M] &= [M_s] + \left(m_{\text{Asym}} + b\right)\left(\{l\}_{n+1}\{l\}_{n+1}^{\text{T}} + \{l\}_{n+1}\{l\}_{j}^{\text{T}}\right) + b\left(\{l\}_{i}\{l\}_{i}^{\text{T}} - \{l\}_{i}\{l\}_{j}^{\text{T}} - \{l\}_{i}\{l\}_{n+1}^{\text{T}} - \{l\}_{n+1}\{l\}_{i}^{\text{T}}\right),\\
[C] &= [C_s] + c_l\left(\{l\}_{n+1}\{l\}_{n+1}^{\text{T}} - \{l\}_{j}\{l\}_{n+1}^{\text{T}}\right),\\
[K(t)] &= [K_s] + \left[k_{nl}x_{\text{Asym}}(t)^2 + 3k_{nl}rx_{\text{Asym}}(t) + \left(3k_{nl}r^2 + k_l\right)\right]\left(\{l\}_{n+1}\{l\}_{n+1}^{\text{T}} - \{l\}_{j}\{l\}_{n+1}^{\text{T}}\right),
\end{aligned}
\tag{8}
$$

where $[M_s]$, $[C_s]$, and $[K_s]$ are $(n+1)$-by-$(n+1)$ matrices formulated by augmenting a row vector and a column vector of zero elements to the bottom and the rightmost of the mass, damping, and stiffness matrices of the uncontrolled structure, respectively. Only the p^{th} $(p = 1,\ldots,n+1)$ element in the $(n+1)$-by-1 vector $\{l\}_p$ is equal to one, while the others are zeros. The superscript T denotes the transposition operation.

Considering the nonlinear terms introduced by Asym NESI, equation (7) is numerically solved by using the incremental Newmark-β method with the Newton–Raphson iteration method at each time step. The initial displacement and velocity of all DOFs are zero. Assuming that the responses of the nonlinear system follow a Gaussian distribution under excitations of weakly stationary wind loads, the extreme value $\widehat{X}$ of displacement and acceleration responses can be estimated based on the sample of time history as follows [39]:

$$\widehat{X} = \overline{X} \pm g\sigma_x, \tag{9}$$

where $\overline{X}$ and σ_x are the mean value and standard deviation of an observation sample, respectively. g is the peak factor evaluated by [40]

$$g = \left[2\ln\left(\eta T_w\right)\right]^{1/2} + \frac{0.577}{\left[2\ln\left(\eta T_w\right)\right]^{1/2}}, \tag{10}$$

where T_w is the time duration of the observation sample and η is the effective frequency for structural responses, which can be conservatively taken to be equal to the first natural frequency of the uncontrolled structure in Hz [40].

Further, a reduction ratio R is defined in equation (11) to quantitatively evaluate the mitigation effects of control devices on the wind-induced responses, where $\widehat{X}_c$ and $\widehat{X}_{\text{uc}}$ are the extreme values of responses of the controlled and uncontrolled structures, respectively.

$$R = \left(1 - \frac{\widehat{X}_c}{\widehat{X}_{\text{uc}}}\right). \tag{11}$$

Having in mind that the performance of passive control devices highly relies on tuning parameters, a sensitivity index S is introduced in equation (12) to evaluate the robustness of R against deviations in tuning parameters.

$$S = \frac{\sum_{j=1}^{J}\left(1 - R_{p,j}/R_{up}\right)^2}{J}, \tag{12}$$

where R_{up} is the reduction ratio of the control device whose parameters are not perturbed and $R_{p,j}$ is the reduction ratio of the control device whose parameters are artificially modified under the j^{th} set of perturbations $(j = 1, \ldots, J)$.

3. Case Study

3.1. Introduction of the High-Rise Building. A high-rise building located in the typhoon-prone areas along the southeast coast of China is taken as the primary structure. The building has a height of 300 m (69 stories) and a weight of 233,840 t. Geometric sizes and the definition of the body axes of the building are presented in Figure 4(a). The wind direction of the approaching wind is denoted as α_w. The lumped mass of each floor and lateral stiffness between consecutive floors are extracted from the finite element (FE)

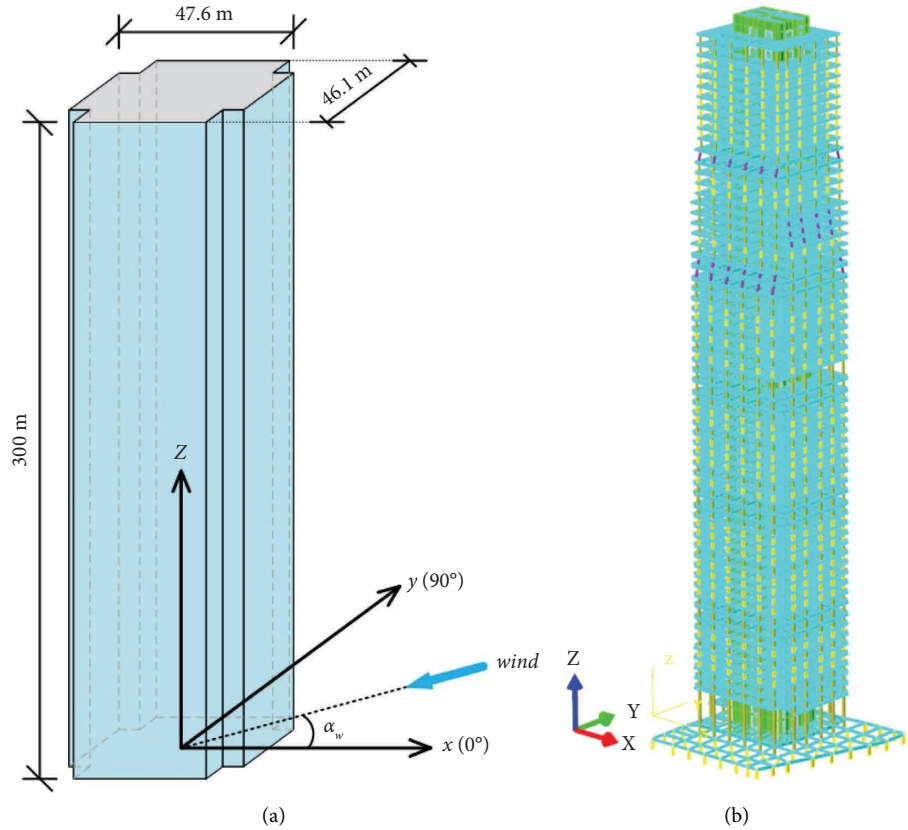

Figure 4: (a) Geometric sizes and (b) FE model of the high-rise buildings.

model shown in Figure 4(b). The FE model is established in YJK®, an FE-based structural analysis software that is commonly used in China.

The distribution of lumped mass along height is shown in Figure 5(a), wherein the jumps in masses of specific floors are attributed to the strengthened structural components and emergency devices of refuge floors. As the lateral stiffness along the y-axis is smaller than that along the x-axis, preliminary analyses of wind-induced responses show that the responses along the y-axis are larger than those along the x-axis. Thus, only the stiffness along the y-axis (cf. Figure 5) is adopted to establish a planar lumped mass model as presented in Figure 1(a). The first natural frequency of the planar model of the high-rise building is $f_1 = 0.143$ Hz, which is close to 0.138 Hz of the FE model. Rayleigh damping is adopted to formulate the damping matrix with an assumed damping ratio of 5% for the first two modes when calculating displacement but a smaller value of 2% when calculating acceleration. This difference is due to the consideration that the wind loads for calculating displacement correspond to a return period of 50 years and are larger than that for calculating acceleration (10-year return period), in which case the structural components are expected to dissipate more energy.

3.2. Wind Loads Obtained from Wind Tunnel Tests. The synchronous multipoint pressure measurement wind tunnel tests on the scaled high-rise building were carried out in the boundary layer wind tunnel laboratory. The geometric scale ratio of the model is 1 : 400. According to the location of the building, the C-type wind field simulating an urban area [41] is generated by roughness elements and spires, as presented in Figure 6(a). The profiles of mean wind velocity and turbulence intensity of the C-type wind field are presented in Figure 6(b), wherein H and U represent an arbitrary height and the corresponding mean wind speed. H_T, U_T, and I_U are the reference height, wind speed at H_T, and turbulence intensity, respectively. A good match between the mean wind speed profile measured in the test and that calculated following the power law with $\alpha = 0.22$ [41] can be observed.

The coordinates of wind directions α_w are shown in Figure 7. Wind pressures are measured at a total of 36 wind directions at an interval of 10°. The specific parameters of the wind tunnel tests are listed in Table 1.

At the wind direction of 0°, time histories of the components of aerodynamic forces acting on the 20th and 60th floors along the y-axis (across-wind loads) are shown in Figure 8. The aerodynamic forces on the 60th floor in Figure 8(b) are mainly contributed by vortex shedding effects and have a mean value of approximately zero. In contrast, Figure 8(a) shows that the mean value of aerodynamic loads on the 20th floor is nonzero, which may be attributed to the aerodynamic interference of the surrounding buildings as shown in Figures 6(a) and 7.

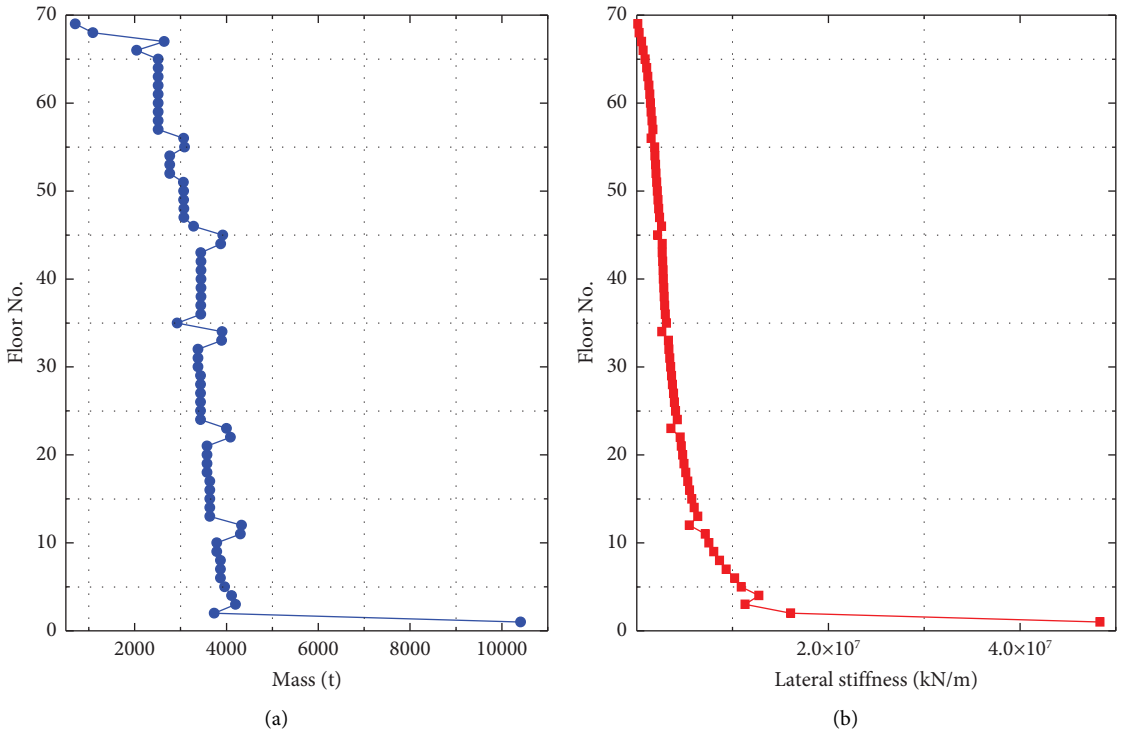

Figure 5: Distribution of (a) lumped masses and (b) lateral stiffness along floors.

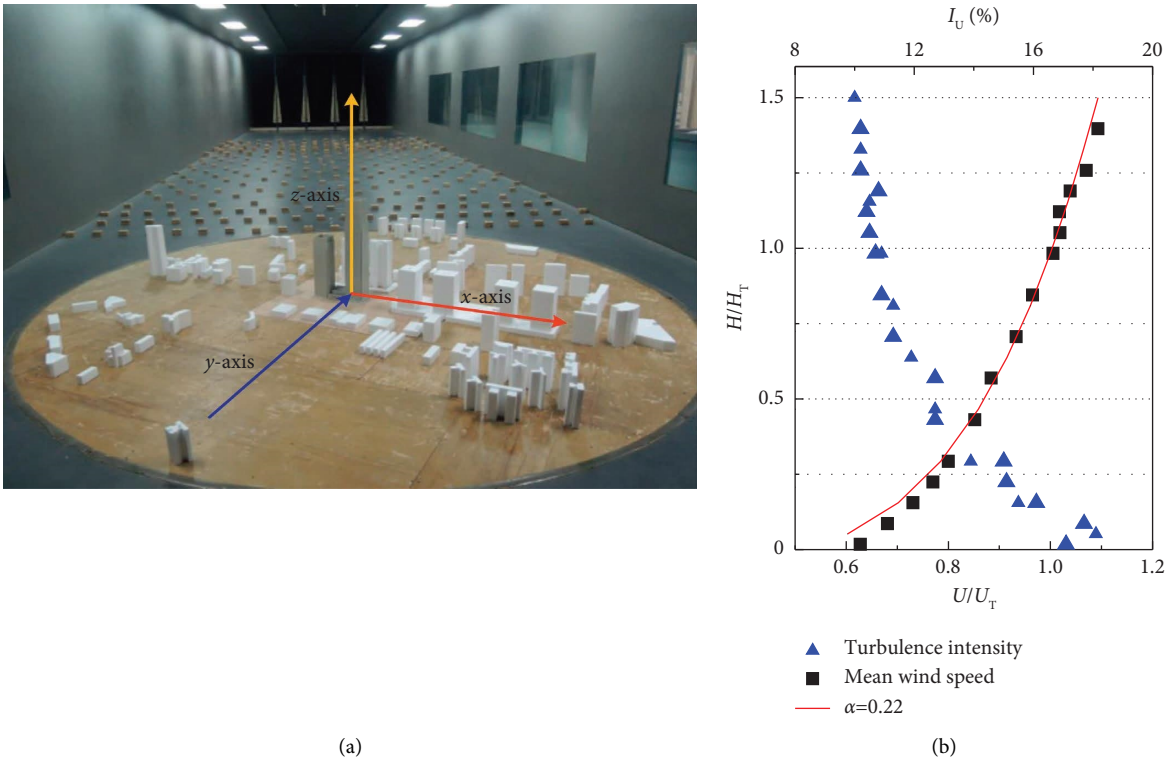

Figure 6: (a) A picture of wind tunnel tests and (b) profiles of the wind field.

Furthermore, power spectral densities (PSDs) of the across- (components along the y-axis at the wind direction of 0°) and along-wind (components along the y-axis at the wind direction of 90°) loads are shown in Figures 9(a) and 9(b) in the dimensionless form, respectively.

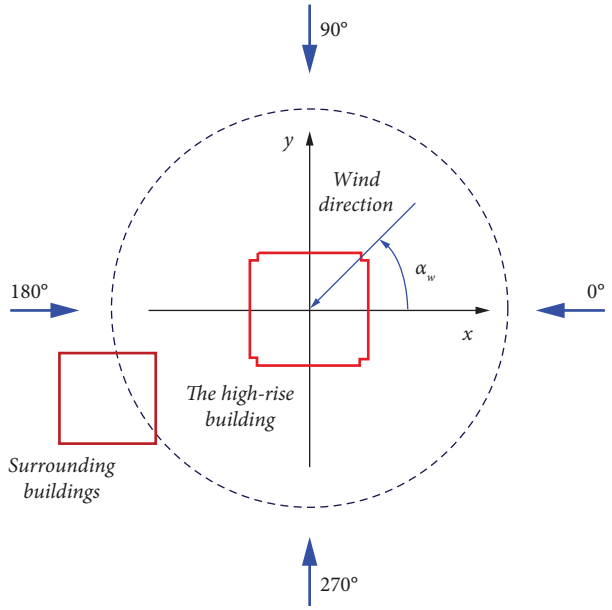

Figure 7: Definitions of wind directions.

Table 1: Parameters of wind tunnel tests.

Geometric scale ratio	Wind speed	Sampling frequency (Hz)	Sampling length	Incremental step	Measuring taps
1 : 400	9.26 m/s	299	20480	10°	264

In Figure 9, f and B represent the frequency and along-wind characteristics length of the building, respectively. $S_p(f)$ and $\sigma_p{}^2$ are the PSD and variance of aerodynamic forces, respectively. Figure 9 indicates that the energy of aerodynamic forces along the across-wind direction is distributed more narrowly than that along the along-wind direction and mainly distributed around the dimensionless frequency of 0.12, corresponding to the Strouhal number for a square cross-section [42].

3.3. Parametric Optimization. To make a fair comparison among the performance of Asym NESI, cubic NESI, and TMDI, parametric optimizations for the three control devices are carried out.

According to Figure 1(b), a total of eight dimensionless parameters of Asym NESI need to be optimized, i.e., mass ratio $\mu = m_{\text{Asym}}/M_{\text{tot}}$ (M_{tot} is the total mass of the primary building), inertance ratio $\beta = b/M_{\text{tot}}$, stiffness ratio of linear spring $\kappa_l = k_l/(m_{\text{Asym}} + b)\omega_1^2$ (ω_1 denotes the first natural circular frequency of the high-rise building), stiffness ratio of nonlinear spring $\kappa_{\text{nl}} = k_{\text{nl}}/(m_{\text{Asym}} + b)\omega_1^2$, the set distance r, damping ratio $\zeta = c_l/2(m_{\text{Asym}} + b)\omega_1$, the installation floor of the Asym NESI j, and the downward spanning floors of inerter $\text{tp} = j - i$ (cf. Figure 1(a)).

Both mitigation effects and robustness at the most unwanted wind direction (0°) are pursued in the optimization, which is reflected by simultaneously minimizing four objectives, i.e., absolute extreme displacement on the top floor $|\widehat{x}_{69}| = |\overline{x}_{69}| + g\sigma_{x69}$, extreme acceleration on the top floor $\ddot{\widehat{x}}_{69} = g\sigma_{\ddot{x}69}$, sensitivity of control performance on displacement responses S_{dis}, and sensitivity of control performance on acceleration responses S_{acc}. Specifically, S_{dis} and S_{acc} are calculated by considering eight sets of perturbations $\{\alpha_Z, \alpha_K\}$ exerted on ζ and κ_{nl} for Cubic NESI and ζ and κ_l for TMDI, i.e., $\zeta_{\text{perturbed}} = \alpha_Z\zeta$, $\kappa_{nl,\text{perturbed}} = \alpha_K\kappa_{nl}$, and $\kappa_{l,\text{perturbed}} = \alpha_K\kappa_l$. The eight sets of perturbations are all permutations of $\alpha_Z = \{0.8, 1.0, 1.2\}$ and $\alpha_K = \{0.8, 1.0, 1.2\}$ except $\alpha_C = \alpha_K = 1.0$. Particularly, perturbations on only ζ and κ_l of Asym NESI are considered in the optimization stage to accelerate the calculation of objectives. Influences of variations in κ_{nl} of Asym NESI will be discussed in Section 3.4.

By referring to the optimal values reported in the literature regarding IVAs and NESIs [24, 25, 32, 34, 36], a constrained multi-objective optimization problem (CMOP) expressed in equation (13) is formulated to mathematically describe the optimization problem. Notably, tp is strictly limited below 5, considering the great practical difficulties in realizing a control device spanning too many floors. The upper bound value 4 is determined by referring to the existing pendulum-like TMDs, e.g., the TMD in Taipei 101 tower (spanning 4 floors) [43] and the eddy current TMD in Shanghai Center Tower (spanning more than 20.6 m) [44].

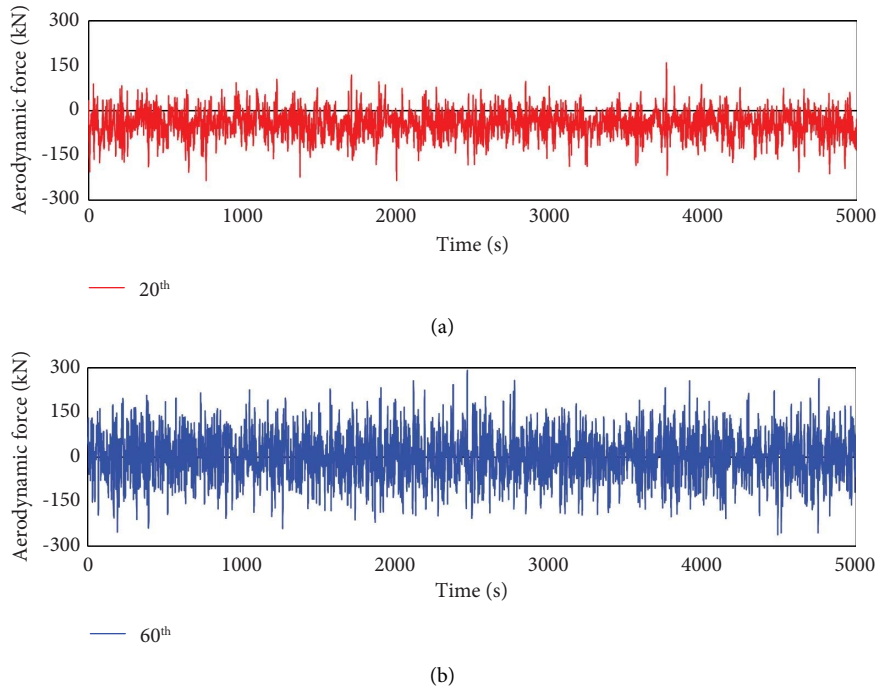

Figure 8: Time histories of aerodynamic forces (a) on the 20th floor and (b) the 60th floor at the wind direction of 0°.

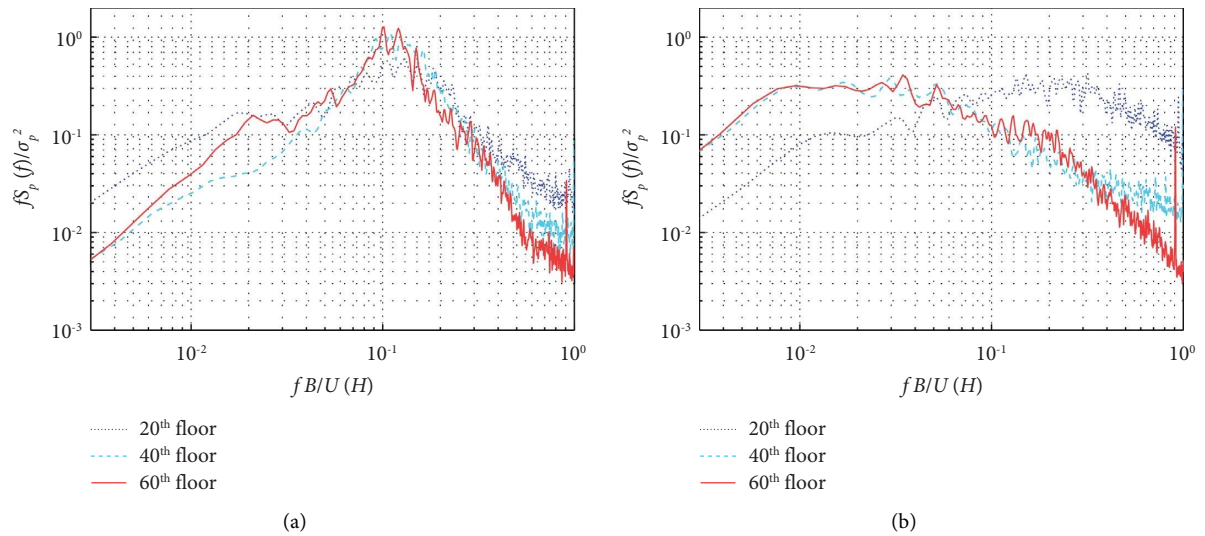

Figure 9: PSDs of aerodynamic forces along the (a) across- and (b) along-wind direction.

$$\text{minimize} \begin{cases} f_1(\mu, \beta, \kappa_l, \kappa_{nl}, r, \zeta, j, tp) = |\hat{x}_{69}|, \\ f_2(\mu, \beta, \kappa_l, \kappa_{nl}, r, \zeta, j, tp) = \hat{\ddot{x}}_{69}, \\ f_3(\mu, \beta, \kappa_l, \kappa_{nl}, r, \zeta, j, tp) = S_{\text{dis}}, \\ f_4(\mu, \beta, \kappa_l, \kappa_{nl}, r, \zeta, j, tp) = S_{\text{acc}}, \end{cases} \tag{13}$$

$$\text{s.t} \begin{cases} \mu \in [0, 0.5\%], \beta \in [0, 1], \kappa_l \in [0, 3], \\ \kappa_{\text{nl}} \in [0, 2500], r \in [0, 0.1], \\ \zeta \in [0, 0.4], j \in \{1, \cdots, 69\}, tp \in \{0, \cdots, 4\}. \end{cases}$$

Similarly, CMOPs for cubic NESI and TMDI are defined under the same constraints. All three CMOPs are solved by using the built-in MATLAB® function, i.e., "gamultiobj," which is a variant of the nondominated sorting genetic algorithm (NSGA-II) [45]. It is noted that the solutions of CMOPs are mostly a set of nondominated individuals having preferences on different objectives (known as the Pareto set), where there does not exist a single solution that can simultaneously achieve minimum (or maximum) on all objectives. The four objectives of solutions form a 4-dimensional (4D) Pareto front (PF) in the objective space,

and radar plots are used to demonstrate the preferences of all optimal individuals on different objectives. To make an intuitive comparison among the objectives of the three devices, the four objectives of the i^{th} individual are transformed into dimensionless form following equations (14)–(17) and shown in Figure 10.

$$r_{1,i} = \frac{\left|\widehat{x}_{69}\right|_i}{\left|\widehat{x}_{69}\right|_{\text{uncontrolled}}}, \tag{14}$$

$$r_{2,i} = \frac{\widehat{\ddot{x}}_{69,i}}{\widehat{\ddot{x}}_{69,\text{uncontrolled}}}, \tag{15}$$

$$r_{3,i} = \frac{S_{\text{dis},i}}{\max\left(\{S_{\text{dis}}\}\right)}, \tag{16}$$

$$r_{4,i} = \frac{S_{\text{acc},i}}{\max\left(\{S_{\text{acc}}\}\right)}, \tag{17}$$

where $|\widehat{x}_{69}|_{\text{uncontrolled}}$ and $\ddot{x}_{69,\text{uncontrolled}}$ are the extreme displacement and acceleration on the top floor of the uncontrolled structure, respectively. $\max(\{S_{\text{dis}}\})$ and $\max(\{S_{\text{acc}}\})$ are the maximum values of S_{dis} and S_{acc} among all optimal individuals of the three control devices, respectively. Besides optimal solutions, positive ideal solution (PIS) and negative ideal solution (NIS) are also depicted to demonstrate the limits of each device on the four objectives. PIS and NIS are generated by collecting the minimal and maximum values of all optimal solutions, respectively. Representatives having a good balance among the four objectives are selected and highlighted in red dash-dot lines for the three control devices.

In Figure 10, Asym NESI and TMDI share a similar PIS, indicating that the performance limits of these two devices on each objective are almost identical. PIS of cubic NESI has a similar r_3 and r_4 to those of Asym NESI and TMDI, but its r_1 and r_2 are larger than those of the other two, which demonstrates that the potentials of cubic NESI on decreasing responses are worse than those of Asym NESI and TMDI. However, r_3 and especially r_4 of NISs of Asym NESI and TMDI are larger than those of cubic NESI, which suggests that cubic NESI could be a better choice when robustness on acceleration control performance is the prior design requirement.

Further, the variations of r_3 and r_4 with respect to r_1 and r_2 of the optimal individuals are shown in Figure 11 by projecting the 4D PF on the r_1–r_3 and r_2–r_4 planes to demonstrate the relationship between mitigation effects and robustness.

In Figure 11(a), the maximum reductions in displacement and acceleration (corresponding to the minimum r_1 and r_3) achieved by Asym NESI and TMDI are close, while cubic NESI is less effective on vibration control than the other two. Between Aysm NESI and TMDI, there mostly exists an optimal individual of Asym NESI that has a similar r_1 or r_2 to that of TMDI with a smaller r_3 or r_4. This indicates that Asym NESI could be an alternative to TMDI for similar mitigation effects but more sound robustness. Although performing poorly on mitigating responses, cubic NESI generally exhibits better robustness on acceleration control, as shown in Figures 10(b) and 11(b).

To provide guidance on the parametric design of NESI for wind-induced vibration control, the optimal parameters and objectives of the three representatives marked in Figure 10 are listed in Tables 2 and 3, respectively.

In Table 2, the optimal β of all three devices is close to or has reached the upper bound of 1, indicating that the incorporation of inerters will enhance the overall performance. Asym NESI and TMDI share similar κ_l and ζ, which signifies that Asym NESI is designed to resonate with the first mode. Besides, κ_{nl} of 67.94 is designed for Asym NESI to enhance its overall performance. In contrast, the optimal κ_{nl} of cubic NESI is significantly larger than κ_l and κ_{nl} of the others, which may hinder its practical implementation. Unlike NES and TMD which are usually designed to be installed on the top [25, 46, 47], all three inerterincorporated control devices are optimized to be installed in the middle portion of the building with a multistory spanning layout, which leverages the enhancement effects of inerters [21, 48].

Further, the objective values of representatives of the three devices are reported in Table 3. As presented in Figure 11, Asym NESI and TMDI have almost identical mitigation effects and outperform cubic NESI in reducing responses. Regarding robustness, the sensitivity indices of cubic NESI on displacement and acceleration control are only 5.5 % and 29.8 % of those of TMDI, respectively, and the corresponding values of Asym NESI are 70.5 % and 62.5 %'.

3.4. Assessment on Mitigation Effects of Asym NESI, Cubic NESI, and TMDI

3.4.1. Amplitude-Frequency Curves. To investigate the dynamic properties of controlled structures over a broad frequency band, the amplitude-frequency relationship for acceleration and displacement responses on the top floor controlled by two NESIs are numerically calculated through harmonically forced vibrations, while the amplitude-frequency curves of the uncontrolled and TMDI-controlled structures (i.e., moduli of frequency response functions for linear systems) are analytically calculated [48]. The results are shown in Figure 12.

Figure 12(a) shows that Asym NESI and TMDI significantly decrease the peak values at the first natural frequency and rationally achieve desirable reductions in displacement responses since the first mode dominates the wind-induced vibration. Cubic NESI failed to effectively reduce the first peak and perform worst among the three. Regarding control performance on higher modes, all three control devices have neglectable reductions on the second peak, and minor decreases on the third peak are observed. Similarly, all three absorbers can decrease the peak value of the amplitude-frequency curve at the first natural frequency in Figure 12(b), and both Asym NESI and TMDI perform better than cubic NESI. Notably, the amplitude-frequency curve of the structure controlled by Asym NESI is almost identical to that of the TMDI-controlled structure in the present case, implying that the whole system behaves almost linearly.

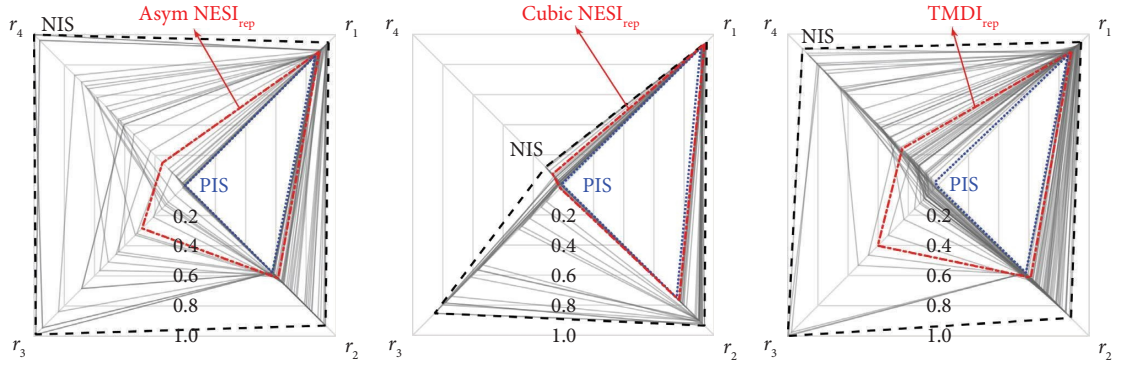

Figure 10: Objective values of optimal (a) Asym NESI, (b) cubic NESI, and (c) TMDI.

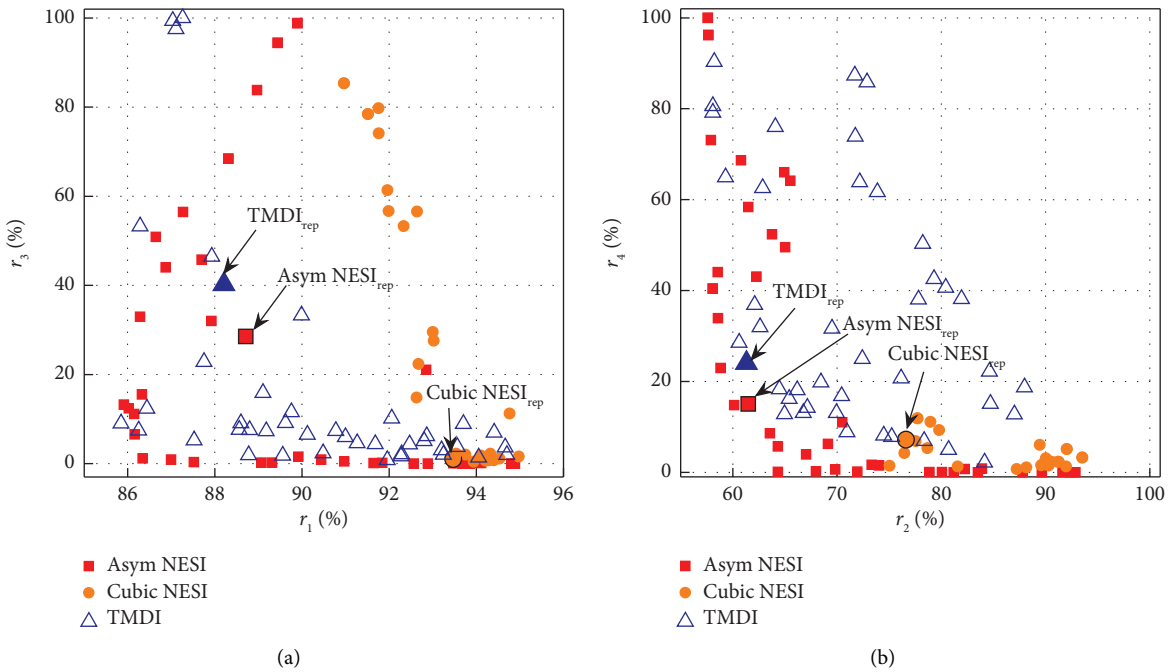

Figure 11: Relationship between (a) r_1 and r_3, and (b) r_2 and r_4.

Table 2: Optimal parameters of the representatives of Asym NESI, cubic NESI, and TMDI.

Control strategy	μ (%)	β	κ_l	κ_{nl}	ζ	r (cm)	j	tp
Asym NESI	0.42	0.99	0.88	67.94	0.16	3.68	38	4
Cubic NESI	0.50	1.00	\	2.31×10^3	0.18	\	35	4
TMDI	0.49	1.00	1.17	\	0.18	\	37	4

Table 3: Objective values of the representatives of Asym NESI, cubic NESI, and TMDI.

Control strategy	$\lvert\hat{x}_{69}\rvert$ (cm)	$\hat{\ddot{x}}_{69}$ (cm/s^2)	S_{dis} ($\times 10^{-4}$)	S_{acc} ($\times 10^{-3}$)
Uncontrolled	30.42	15.60	\	\
Asym NESI	26.98	9.60	6.48	2.43
Cubic NESI	28.45	11.95	0.50	1.16
TMDI	26.83	9.57	9.14	3.89

3.4.2. Wind-Induced Acceleration Responses. Figures 13(a) and 13(b) present a 10-minute segment of the time histories of the acceleration responses on the top floor of the high-rise building at wind directions of 0° and 90°, respectively.

In Figure 13, all three absorbers can decrease acceleration responses at both wind directions, wherein Asym NESI has identical performance as TMDI and outperforms Cubic NESI. Between the two wind directions, the control performance of three devices on across-wind vibration is better

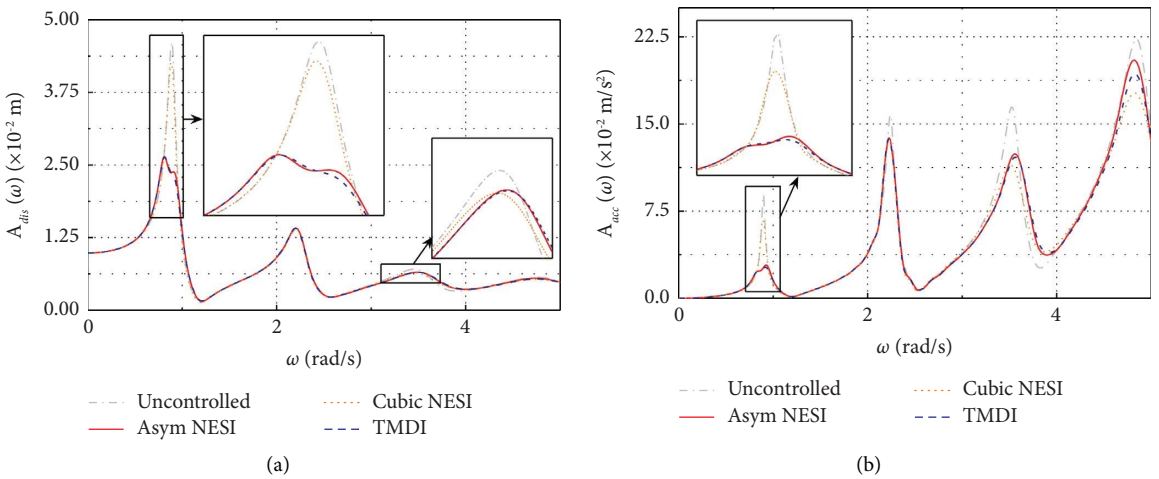

FIGURE 12: Amplitude-frequency curves of (a) displacement and (b) acceleration responses on the top floor under harmonic excitation (amplitude = 2.5×10^5 N) acting on the top floor.

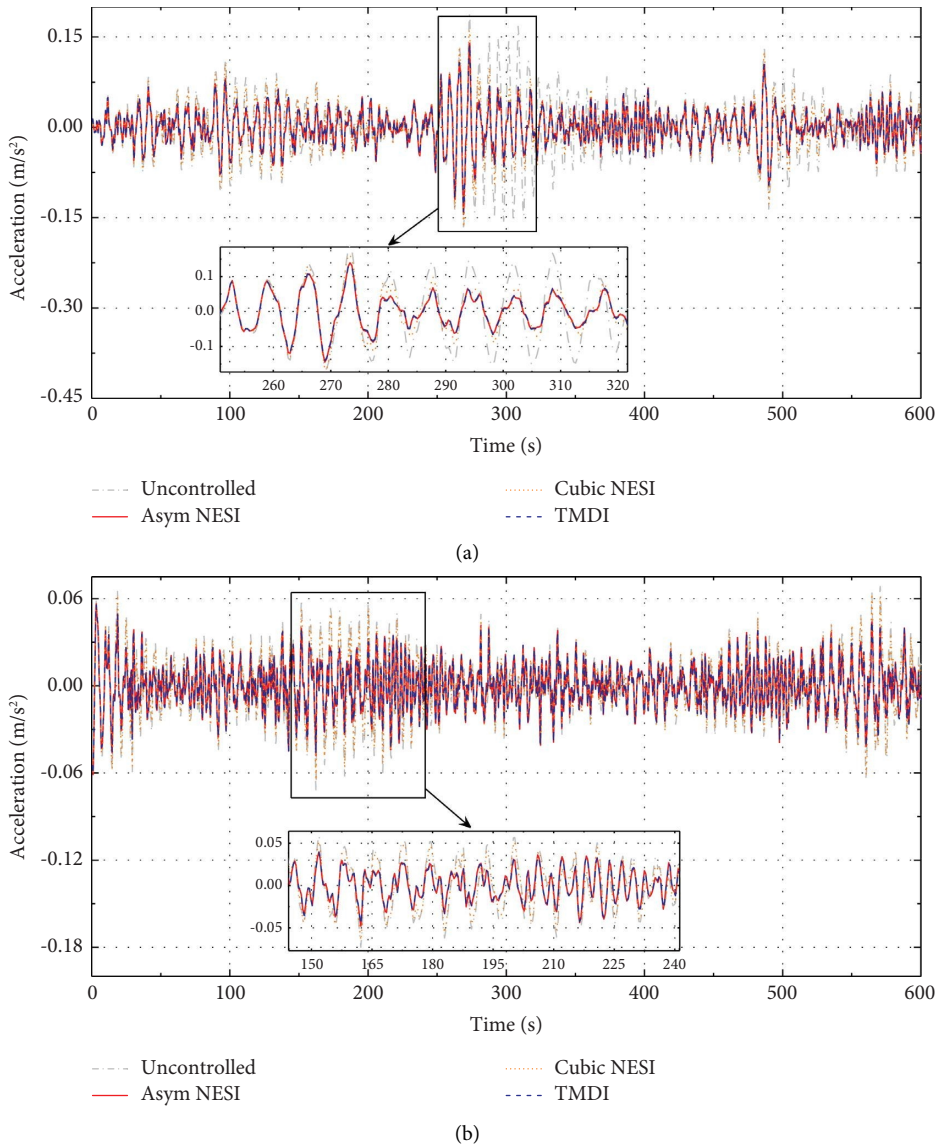

FIGURE 13: Time histories of acceleration responses on the top floor at wind directions of (a) 0° and (b) 90°.

than that on along-wind vibration. This can be explained by observing Figures 9 and 12; that is, the resonant components contribute more to the across-wind responses and can be mitigated to a larger extent due to the significant reduction in amplitude-frequency curves in Figure 12(b). In contrast, the contribution of background components to the along-wind responses is larger than that to across-wind responses. Thus, the minor reduction in amplitude-frequency curves at low frequencies leads to worse control performance than that on across-wind responses.

Further, extreme wind-induced acceleration responses on the top floor at all 36 wind directions are estimated and shown in Figure 14.

In Figure 14, all three control devices can reduce the extreme acceleration responses of the high-rise building at all wind directions. Among the three, Asym NESI and TMDI show desirable mitigation effects at all wind directions, while cubic NESI can only achieve moderate reductions around 0°. $\widehat{\ddot{x}}_{69}$ at typical wind directions at 0°, 90°, 180°, and 270° is further provided in Table 4. Corresponding reduction ratios R are calculated via equation (11) and reported in the parenthesis. As explained before, the mitigation effects of the three devices on across-wind responses are better than those on along-wind responses.

Figures 15(a) and 15(b) show the variation of extreme acceleration along the height at wind directions of 0° and 90°, respectively. Asym NESI shares similar control performance as TMDI and effectively decrease $\widehat{\ddot{x}}$ from the middle-lower portion to the top of the building at the two wind directions. In contrast, cubic NESI shows moderate mitigation effects at the wind direction of 0° but exhibits poor mitigation effects at the wind direction of 90°.

3.4.3. Wind-Induced Displacement Responses. Figures 16(a) and 16(b) show 10-minute segments of the time histories of wind-induced displacement on the top floor at wind directions of 0° and 90°, respectively.

Similar to the results in Figure 13, Asym NESI shares almost identical performance as TMDI, and both control devices outperform cubic NESI. In comparison to control performance on acceleration responses, only moderate reductions at the wind direction of 0° are achieved by the three devices, and limited mitigation effects at the wind direction of 90° are observed. The worse control performance on displacement than that on acceleration can be explained via Figure 12. Specifically, the amplitude-frequency curves at low frequency in Figure 12(a) are horizontal, which makes the contribution of background components to displacement responses larger than that to acceleration responses, and thus result into worse mitigation effects.

Since $|\widehat{\ddot{x}}_{69}| = |\overline{\ddot{x}}_{69}| + g\sigma_{\ddot{x}69}$, the variations of $|\overline{\ddot{x}}_{69}|$ and $g\sigma_{\ddot{x}69}$ along 36 wind directions are separately shown in Figure 17.

In Figure 17(a), the three passive vibration absorbers fail to reduce mean responses. The mean displacement around 0° and 180° approaches zero, since the wind loads are mainly generated by the vortex shedding effects and have an approximately zero mean. In contrast, reductions in STD value attributed to the fluctuating components are observed at all directions in Figure 17(b). Similar to the mitigation effects on acceleration responses, the three control devices perform better at 0° and 180° than 90° and 270° (reported in Table 5), as the mean responses contribute more to along-wind responses than across-wind responses.

Further, the variations of extreme displacement along the height of the building at the wind directions of 0° and 90° are depicted in Figure 18. Differences in control performance on across- and along-wind responses are observed again and not discussed for the sake of brevity.

3.5. Robustness Analysis. Considering the great uncertainties embedded in the dynamic characteristics of super high-rise buildings due to construction, aerodynamic stiffness, aerodynamic damping, and other factors, the control performance of the vibration absorbers probably suffers deterioration due to detuning. To evaluate the influences of detuning on the mitigation effects, $21 \times 21 - 1 = 440$ sets of perturbations are exerted to ζ and κ_l for TMDI and ζ and κ_{nl} for cubic NESI. Differently, Asym NESI has three tuning parameters, i.e., ζ, κ_l, and κ_{nl}, and a total of $441 \times 21 - 1 = 9260$ sets of permutation are considered. Same as the calculation of robustness indices, the 440 sets of perturbations for TMDI and cubic NESI are all permutations of $\alpha_Z = 0.8 : 0.02 : 1.2$ and $\alpha_K = 0.8 : 0.02 : 1.2$ except for $\alpha_Z = \alpha_K = 1.0$. An additional vector of permutation coefficient $\alpha_{Knl} = 0.8 : 0.02 : 1.2$ is considered for κ_{nl} of Asym NESI.

To quantitatively analyze the robustness of these vibration absorbers, a performance index of perturbed control device is defined as

$$\mathrm{PI} = \frac{R_p}{R_{\mathrm{up}}}, \tag{18}$$

where R_p and R_{up} are the reduction ratios of the vibration absorber whose optimal parameters (cf. Table 2) are perturbed or not, respectively, at the wind direction of 0°. Following this definition, PI < 1 indicates that the mitigation effect is weakened, and an enhancement effect is achieved when PI > 1.

Figure 19 shows the variation of PI of Asym NESI, cubic NESI, and TMDI for displacement and acceleration control with α_Z, α_K, and α_{Knl}.

In Figure 19, Asym NESI and TMDI are sensitive to variations in α_K but get less influenced by a changing α_Z. Between the two, Asym NESI shows better robustness on both displacement and acceleration control in terms of minor variations in PI in Figures 19(a) and 19(d) than TMDI (cf. Figures 19(c) and 19(f)). Differently, the robustness of cubic NESI is almost equally affected by both α_Z and α_{Knl} as the contour lines share an inclined angle of about 45°. By comparing the values of PI, cubic NESI shows overall better robustness than Asym NESI and TMDI except for the left-upper zone in Figure 19(e).

Particularly, the influences of κ_{nl} on PI are shown in Figure 20.

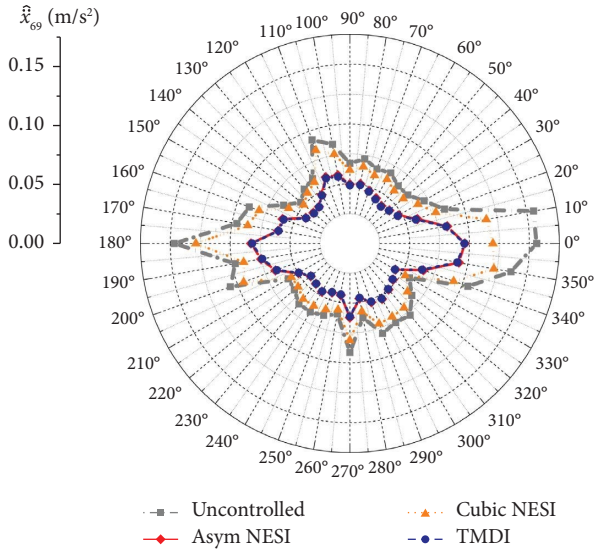

Figure 14: Distribution of $\ddot{\hat{x}}_{69}$ at 36 wind directions.

Table 4: $\ddot{\hat{x}}_{69}$ (cm/s^2) and R (%) at wind directions of 0°, 90°, 180°, and 270°.

Control strategy	Wind directions			
	0°	90°	180°	270°
Uncontrolled	15.60	6.69	14.67	9.11
Asym NESI	9.60 (38.5)	4.95 (26.1)	8.26 (43.7)	6.19 (32.1)
Cubic NESI	11.95 (23.4)	6.15 (8.2)	12.85 (12.4)	8.10 (11.1)
TMDI	9.57 (38.7)	4.88 (27.1)	8.16 (44.4)	6.10 (33.1)

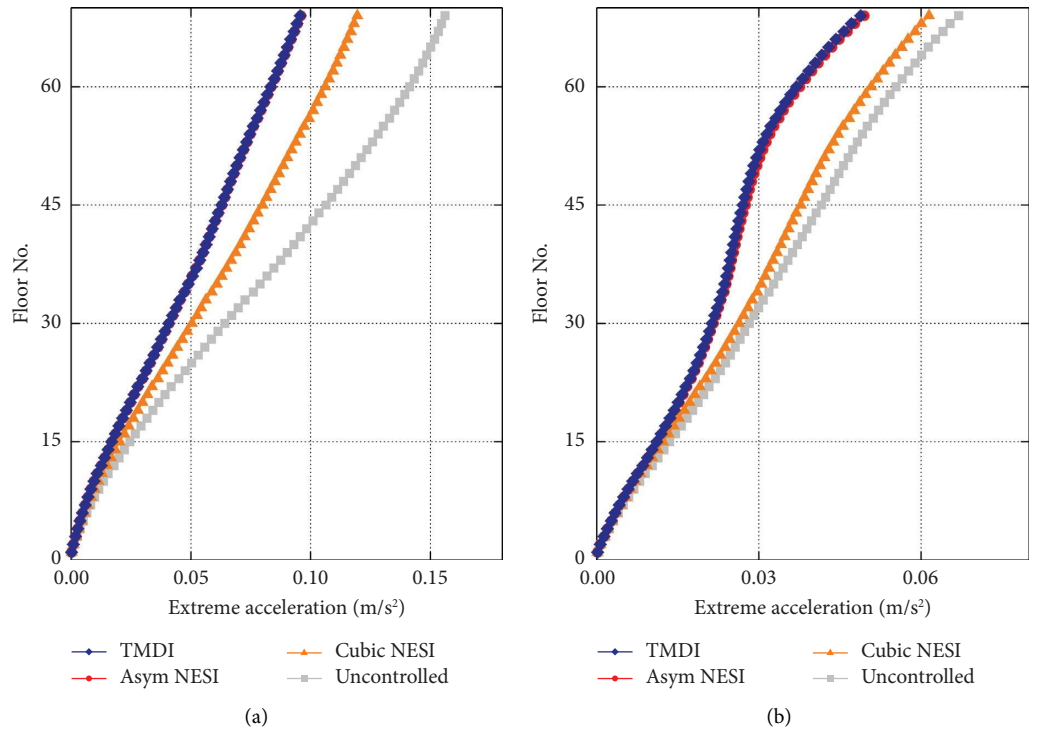

Figure 15: Variation of extreme acceleration along the height at wind directions of (a) 0° and (b) 90°.

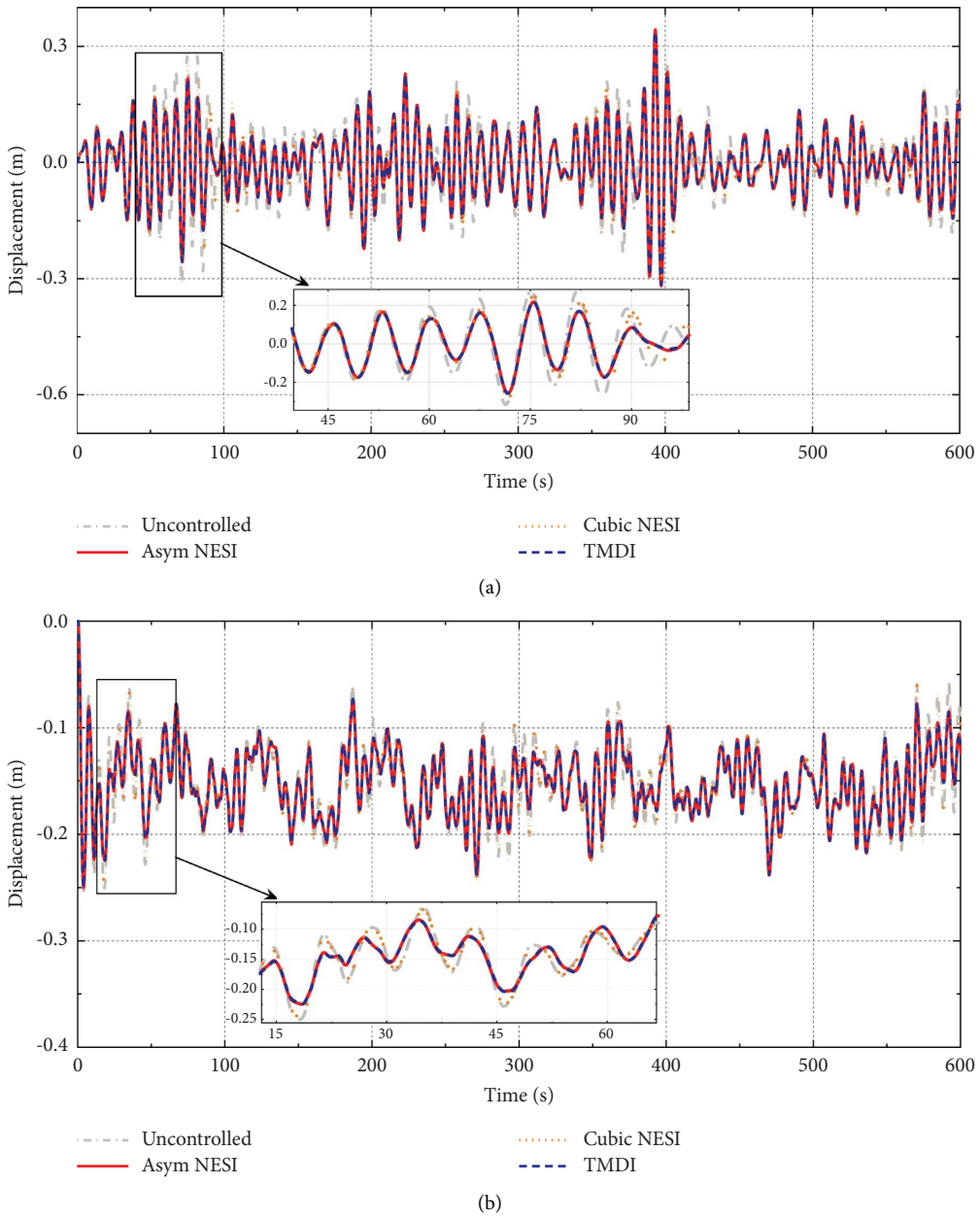

FIGURE 16: Time histories of displacement on the top floor at wind directions of (a) 0° and (b) 90°.

In Figure 20 ($\alpha_{Knl} = 1.0$) and Figures 20(a) and 20(d), the valleys corresponding to low values move downward with an increasing α_{Knl}. Since the stiffness ratio is still tuned beside the first-order frequency of the structure under $\alpha_K = 0.8 : 1.2$, which makes the resonance of Asym NESI with the first mode of the structure the main contributor to the control performance, Asym NESI still exhibits a larger sensitivity to variations in κ_l than ζ.

In addition, it is noticed in Figure 11(b) that an optimum Asym NESI reaches a reduction ratio of 35.7% on acceleration with a marginal S_{acc} of 1.68×10^{-5}, which is much smaller than those reported in Table 3. Although this individual can only decrease the extreme displacement to 27.94 cm, the desirable mitigation effects and sound robustness makes it an attractive choice from the perspective of demand-based design when controlling acceleration is of the greatest concern. The parameters of this individual are listed in Table 6.

From Table 6, this Asym NESI has a much smaller κ_l of only 0.02 in comparison to 0.88 of Asym $NESI_{rep}$. In this way, the nonlinear nature of Asym NESI is expected to be more evident, and its robustness against variations in κ_l is rationally enhanced.

Further, the variations of PI of this Asym NESI with α_Z, α_K, and α_{Knl} for displacement and acceleration control are shown in Figure 21.

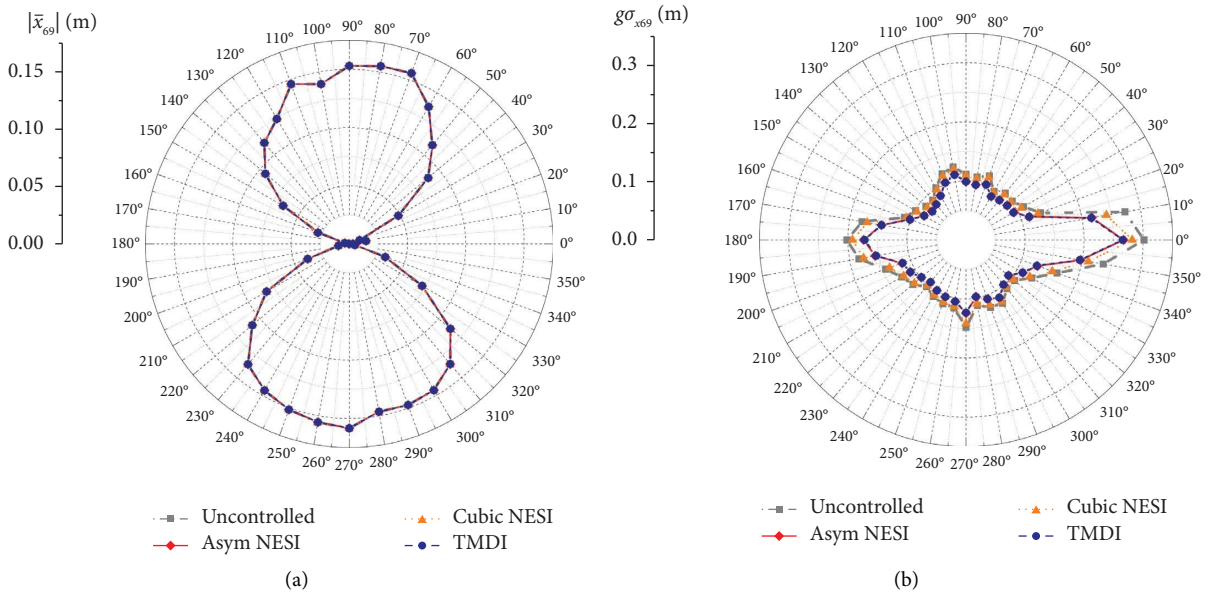

Figure 17: Variations of (a) $|\bar{x}_{69}|$ and (b) $g\sigma_{x69}$ at 36 wind directions.

Table 5: $|\hat{x}_{69}|$ (cm) and R (%) at wind directions of 0°, 90°, 180°, and 270°.

Control strategy	Wind directions			
	0°	90°	180°	270°
Uncontrolled	30.42	26.42	20.15	30.31
Asym NESI	26.98 (11.3)	25.18 (4.7)	17.34 (13.9)	28.21 (6.9)
Cubic NESI	28.45 (6.5)	26.16 (1.0)	19.22 (4.6)	29.96 (1.2)
TMDI	26.83 (11.8)	25.17 (4.8)	17.19 (14.7)	28.15 (7.1)

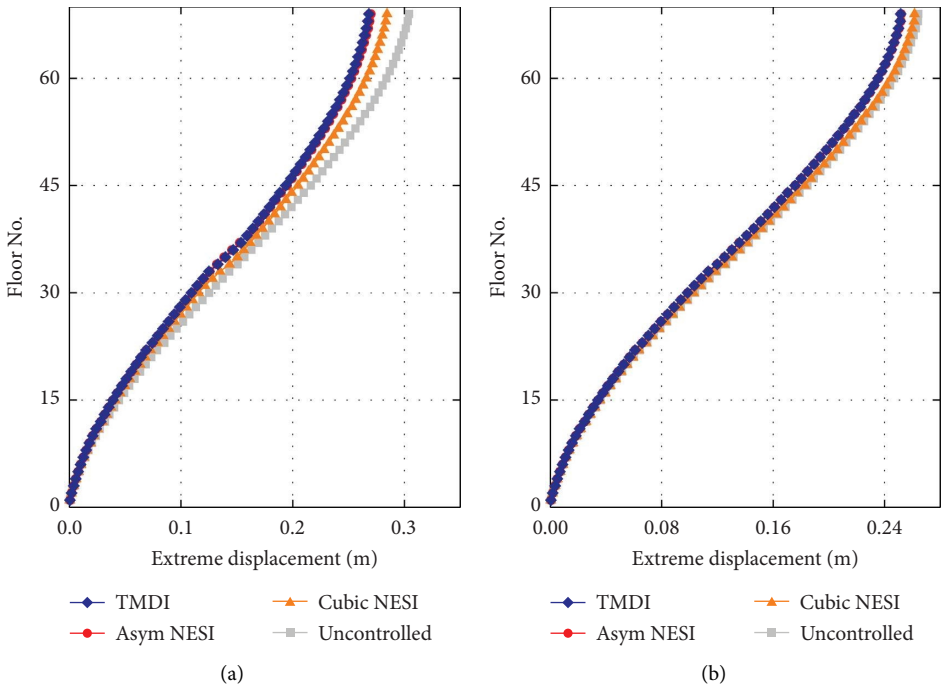

Figure 18: Variation of extreme displacement along the height at wind directions of (a) 0° and (b) 90°.

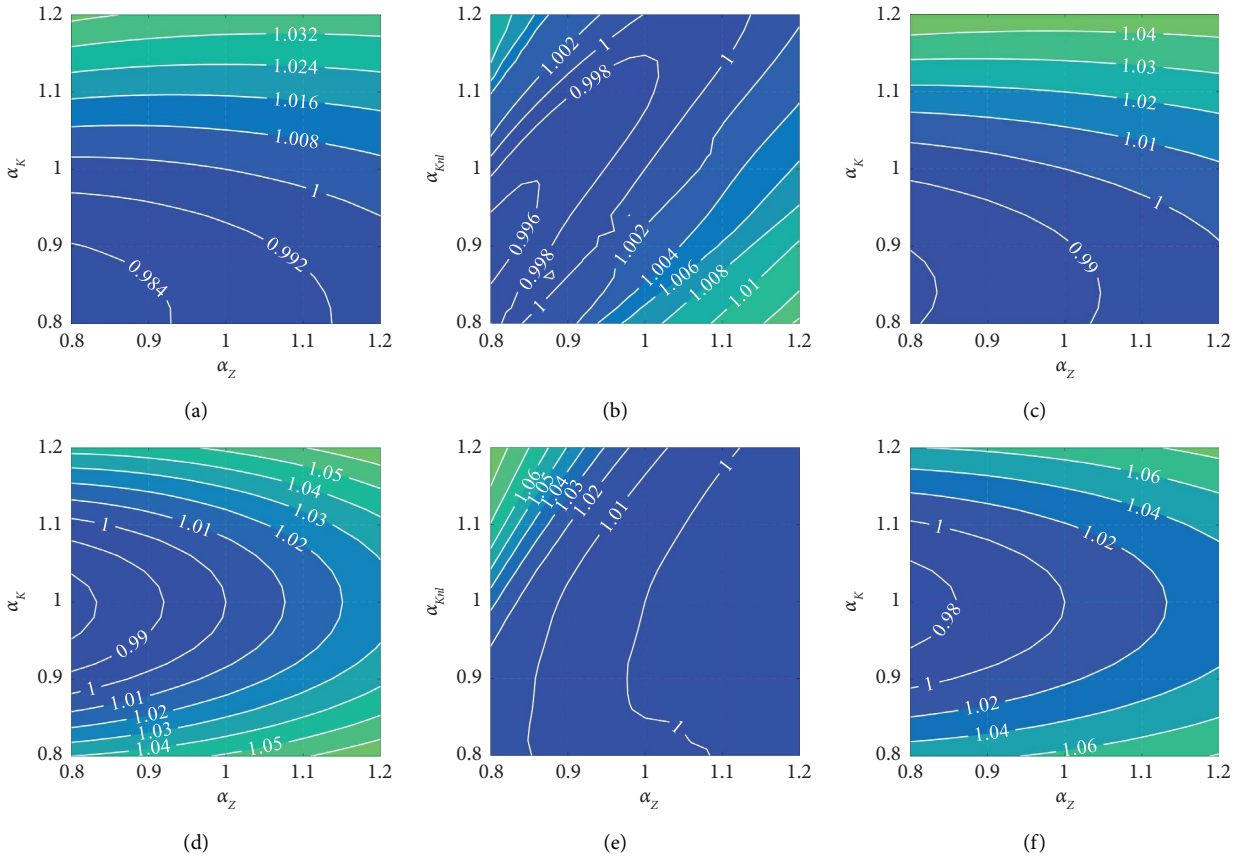

FIGURE 19: Variations of PI of (a) Asym NESI, (b) cubic NESI, and (c) TMDI with α_Z, α_K, and α_{Knl} for displacement control; variations of PI of (d) Asym NESI, (e) cubic NESI, and (f) TMDI with α_Z, α_K, and α_{Knl} for acceleration control.

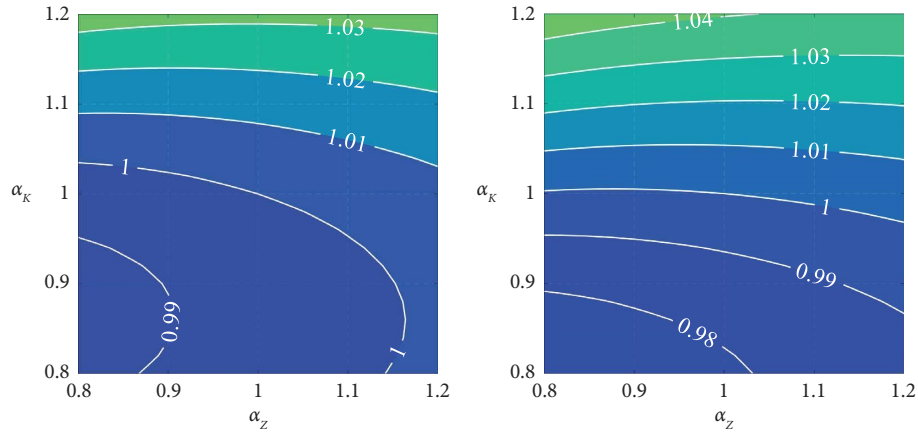

FIGURE 20: Continued.

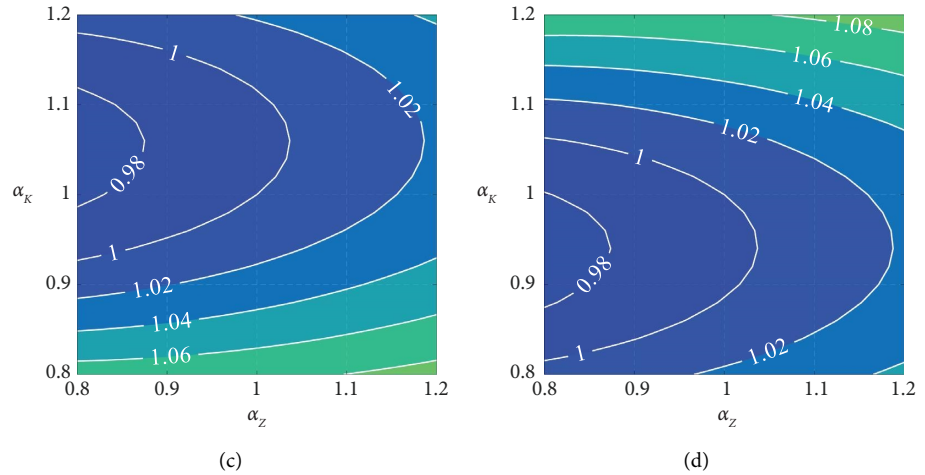

Figure 20: Variations of PI of Asym NESI (cf. Table 2) with α_Z and α_K when (a) $\alpha_{Knl} = 0.8$ and (b) $\alpha_{Knl} = 1.2$ for displacement control; variations of PI of Asym NESI (cf. Table 2) with α_Z and α_K when (c) $\alpha_{Knl} = 0.8$ and (d) $\alpha_{Knl} = 1.2$ for acceleration control.

Table 6: Parameters of an Asym NESI having desirable mitigation effects and sound robustness on acceleration control.

Control strategy	μ (%)	β	κ_l	κ_{nl}	ζ	r (cm)	j	tp
Asym NESI	0.46	0.99	0.02	67.82	0.12	8.52	56	4

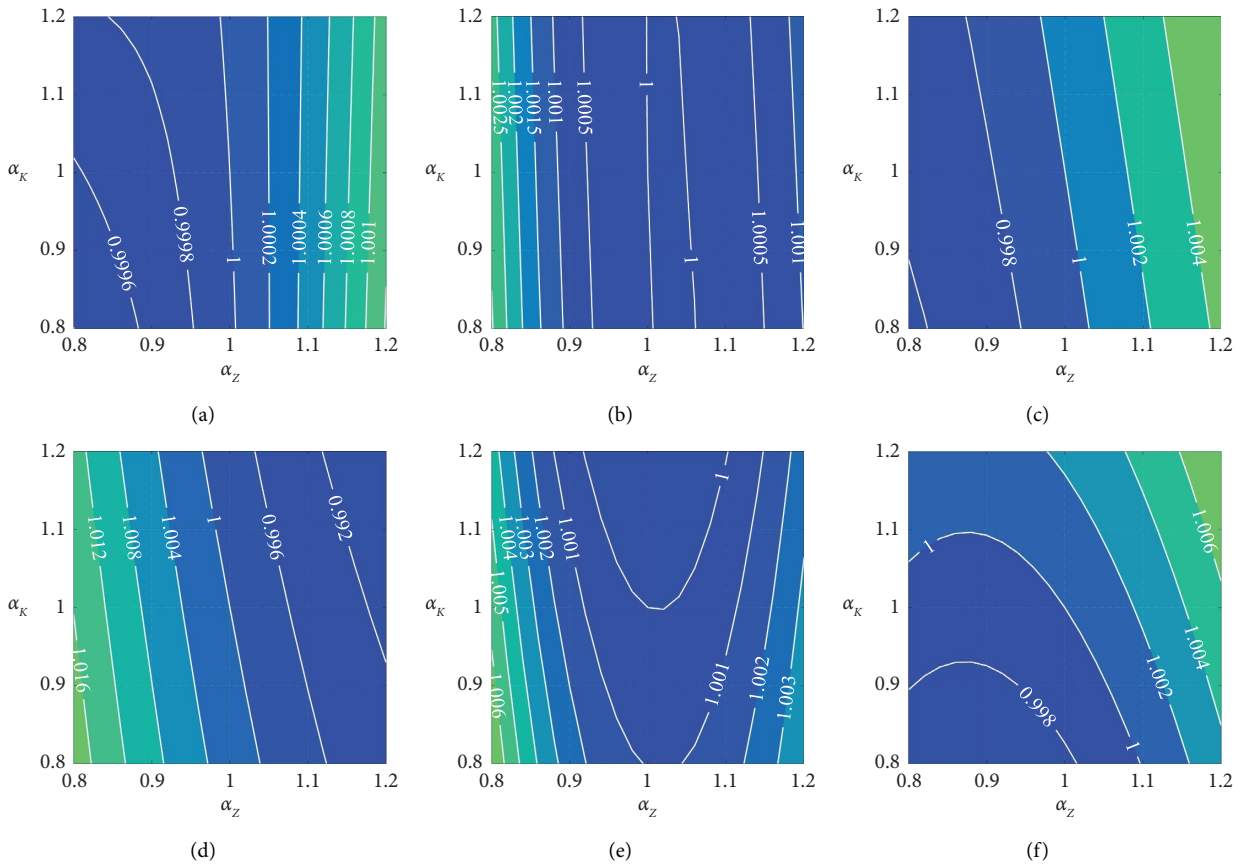

Figure 21: Variations of PI of Asym NESI (cf. Table 6) with α_Z and α_K when (a) $\alpha_{Knl} = 0.8$, (b) $\alpha_{Knl} = 1.0$, and (c) $\alpha_{Knl} = 1.2$ for displacement control; variations of PI of Asym NESI (cf. Table 6) with α_Z and α_K when (d) $\alpha_{Knl} = 0.8$, (e) $\alpha_{Knl} = 1.0$, and (f) $\alpha_{Knl} = 1.2$ for acceleration control.

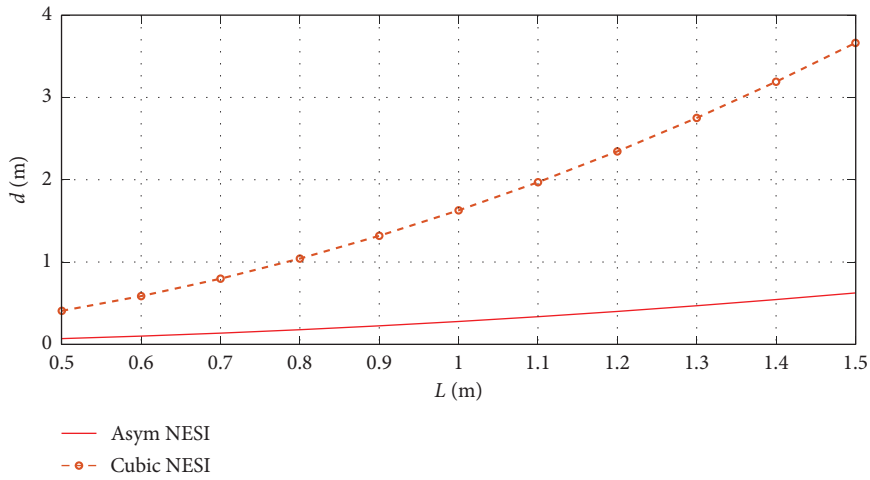

FIGURE 22: L and d for realizing nonlinear springs of NESIs.

As expected, this Asym NESI shows much better robustness in controlling both displacement and acceleration responses than Asym NESI_{rep}, which is reflected by the maximum and minimum values of contour lines. Different from the results in Figures 19 and 20, this Asym NESI is more sensitive to variations in ζ and less sensitive to variations in κ_l, as contour lines which are almost vertical in most figures.

3.6. Practical Considerations. The feasibility of manufacturing the nonlinear spring and the cost of the introduced control devices are further discussed for possible implementation.

According to Table 2, k_{nl} of Asym NESI and cubic NESI is 1.27×10^7 and 4.37×10^8 kN/m, respectively, and k_l of Asym NESI is 1.65×10^5 kN/m. When a metal cable having a circular cross-section with a diameter of d is used to provide the stiffness of $k = E\pi d^2/4$ in the nonlinear spring, we have $d = 2L\sqrt{k_{nl}/\pi E}$ (cf. equation (3)), where E is Young's modulus of the material. Taking steel with $E = 210$ GPa as an example, the relationship between the diameter and length of cable (i.e., d and L) to realize the nonlinear stiffness k_{nl} is shown in Figure 22.

In Figure 22, the required d of Asym NESI is 1/5.87 that of cubic NESI, indicating that the incorporation of an additional linear spring significantly alleviates the high requirement of a large k_{nl} and makes it easier to manufacture the nonlinear spring of Asym NESI than cubic NESI. Although an excessive d is still required for both devices when L is large, multiple parallel cables can be adopted to decrease the diameter of individual cables for easy realization.

Subsequently, the initial (upfront) cost of considered three control devices is assessed in terms of two nonmonetary metrics, i.e., device mass and the maximum output forces of mechanical components [49–51]. The evaluation on other terms of life-cycle cost, e.g., maintenance cost, falls beyond the scope of the present work and is not analyzed.

From Table 2, Asym NESI owns the lightest auxiliary mass which is 84.0% and 85.7% of cubic NESI and TMDI, respectively. The inerters of the three control devices share almost identical inertance. The maximum output forces of the four components, i.e., inertial force of inerter F_I, damping force of dashpot element F_D, restoring force of nonlinear spring F_{Rnl}, and restoring force of linear spring F_{Rl}, are calculated under wind loads at a return period of 50 years following equations (19)–(22).

$$F_I = b \times \max_{0^\circ \le \alpha_w \le 350^\circ} \left| \ddot{x}_{j,\alpha_w} + \ddot{x}_{\text{Asym},\alpha_w} - \ddot{x}_{j-tp,\alpha_w} \right|, \tag{19}$$

$$F_D = c \times \max_{0^\circ \le \alpha_w \le 350^\circ} \left| \dot{x}_{\text{Asym},\alpha_w} \right|, \tag{20}$$

$$F_{Rnl} = k_{nl} \times \max_{0^\circ \le \alpha_w \le 350^\circ} \left| x_{\text{Asym},\alpha_w} + r \right|^3, \tag{21}$$

$$F_{Rl} = k_l \times \max_{0^\circ \le \alpha_w \le 350^\circ} \left| x_{\text{Asym},\alpha_w} - x_l \right|, \tag{22}$$

where $\ddot{x}_{j,\alpha_w}$, $\ddot{x}_{\text{Asym},\alpha_w}$, and $\ddot{x}_{j-tp,\alpha_w}$ are the acceleration time histories of j^{th} DOF, DOF of the floor on which Asym NESI is installed, and $(j-\text{tp})^{\text{th}}$ DOF at the wind direction of α_w, respectively. The dots over characters indicate time derivative. $x_l = k_{nl}r^3/k_l$ is the stretched length of the linear spring at the static balance point. All 36 wind directions from 0° to 350° are considered.

Following equations (19)–(22), the maximum output forces of the four mechanical elements in the three devices at all wind directions are calculated and listed in Table 7.

From Table 7, F_I and F_D of Asym NESI are 102.5% and 111.5% times those of cubic NESI, respectively, but F_{Rnl} of Asym NESI is only 52.8% that of cubic NESI. Although F_{Rl} of Asym NESI is also 74.3% of F_{Rnl} of cubic NESI, the easier realization of a linear spring than a nonlinear one makes Asym NESI more attractive than cubic NESI. In comparison to TMDI, F_D and F_{Rl} of Asym NESI are 90.0% and 94.7% of those of corresponding values, while its F_I is 123.1% of that of TMDI. Generally speaking, TMDI requires the lowest initial cost among the three, assuming that realization of 1 N of the four forces needs the same cost. Considering that the cost of realizing F_{Rnl} is probably larger than realizing F_{Rl}, Asym

Table 7: Maximum output forces of the four mechanical components.

Device	F_I (kN)	F_D (kN)	F_{Rnl} (kN)	F_{Rl} (kN)
Asym NESI	1.65×10^4	3.60×10^3	8.81×10^3	1.24×10^4
Cubic NESI	1.61×10^4	3.23×10^3	1.67×10^4	\
TMDI	1.34×10^4	4.00×10^3	\	1.31×10^4

NESI would be superior to cubic NESI due to a much smaller F_{Rnl}.

4. Conclusions

This paper scrutinized the mitigation effects and robustness of Asym NESI and cubic NESI on wind-induced vibration of high-rise buildings in terms of a detailed numerical case study with TMDI being set as a competitor. The detailed findings are summarized below.

Due to the great difficulties in analytically investigating the nonlinear dynamic behaviors of NESI-controlled MDOF structure, numerical integration and numerical search algorithm are employed to solve the CMOPs targeting both mitigation effects and robustness to obtain the optimal parameters of Asym NESI, cubic NESI, and TMDI. The optimization results show that Asym NESI and TMDI can significantly reduce the extreme displacement and acceleration on the top floor at the most unwanted wind direction. Benefiting from the nonlinear stiffness, Asym NESI exhibits better robustness against perturbations on the design parameters than TMDI having the same mitigation effects. Cubic NESI achieves overall the best robustness on displacement and acceleration control at the cost of the worst mitigation effects on responses and a much larger nonlinear stiffness than that of Asym NESI.

Three representatives of Asym NESI, cubic NESI, and TMDI are selected in terms of a good balance between mitigation effects and robustness. The representative Asym NESI has an optimal κ_l of 0.88, which is close to $\kappa_l = 1.14$ of TMDI. The optimal κ_{nl} of Asym NESI is 62.7 and significantly smaller than 2.31×10^3 of cubic NESI. The optimal mass and inertance ratios of the three devices are close to or have reached the upper bound, indicating that a larger effective mass contributes to overall better performance. Attributed to the incorporation of inerter, the optimal installation layout of the three inerter-integrated devices is to be installed in the middle portion of the structure and spanning multiple floors.

Regarding mitigating effects, the three vibration absorbers can mitigate the wind-induced responses at all 36 wind directions. The reduction ratios of the three representatives on extreme displacement are 11.3%, 6.5%, and 11.8% at the wind direction of 0°, respectively, and corresponding reduction ratios on extreme acceleration are 38.5%, 23.4%, and 38.7%. At the wind direction of 90° (along-wind direction of the structure), the reduction ratios of the three control devices on extreme acceleration decrease to 26.1%, 8.2%, and 27.1%, respectively, and the corresponding values on extreme displacement are only 4.7%, 1.0%, and 4.8%. These differences are mainly attributed to the distinct distribution of energy of across- and along-wind loads and the dynamic behaviors of the controlled structure.

By artificially changing ζ, κ_l, and κ_{nl}, the robustness of the three optimum representatives is evaluated. The sensitivity indices of Asym NESI on displacement and acceleration responses are 70.5% and 62.5% of those of TMDI having the same reduction ratios. Cubic NESI shows better robustness than Asym NESI but exhibits poor mitigation effects. Considering both control performance and optimal parameters, Asym NESI could be an alternative to TMDI due to the competitive mitigation effects but better robustness against detuning.

Since extreme acceleration is more concerned in wind-resistant design, the robustness of an optimum Asym NESI having a reduction ratio of 35.7% but extraordinary robustness on acceleration control is particularly assessed. In comparison to the representative Asym NESI having balanced performance on all objectives with a $\kappa_l = 0.88$, the results suggest that adopting an Asym NESI with a small $\kappa_l = 0.02$ could result in considerable enhancement in robustness at the cost of minor deterioration on acceleration control performance.

Practicality analyses indicate that the incorporation of a linear spring in Asym NESI effectively reduces its realization difficulty in comparison to cubic NESI and probably makes Asym NESI more cost-effective than cubic NESI. TMDI is also attractive due to its desirable control performance and low initial cost evaluated in terms of device mass and maximum output forces of mechanical components.

Data Availability

The data used to support the findings of this study are available from the corresponding author upon request.

Conflicts of Interest

The authors declare that they have no conflicts of interest.

Acknowledgments

This research was funded by the State Key Laboratory of Disaster Reduction in Civil Engineering (Grant no. SLDRCE21-06) at Tongji University, National Natural Science Foundation of China (Grant no. 52278536) and Natural Science Foundation of Southwest University of Science and Technology (Grant no. 21zx7150) which are gratefully acknowledged.

References

[1] M. Jafari and A. Alipour, "Methodologies to mitigate wind-induced vibration of tall buildings: a state-of-the-art review," *Journal of Building Engineering*, vol. 33, Article ID 101582, 2021.

[2] S. Liang, S. Liu, Q. S. Li, L. Zhang, and M. Gu, "Mathematical model of acrosswind dynamic loads on rectangular tall buildings," *Journal of Wind Engineering and Industrial Aerodynamics*, vol. 90, no. 12-15, pp. 1757–1770, 2002.

[3] R. Ma, K. Bi, and H. Hao, "Inerter-based structural vibration control: a state-of-the-art review," *Engineering Structures*, vol. 243, Article ID 112655, 2021.

[4] Z. Lu, Z. X. Wang, Y. Zhou, and X. L. Lu, "Nonlinear dissipative devices in structural vibration control: a review," *Journal of Sound and Vibration*, vol. 423, pp. 18–49, 2018.

[5] M. Gutierrez Soto and H. Adeli, "Tuned mass dampers," *Archives of Computational Methods in Engineering*, vol. 20, no. 4, pp. 419–431, 2013.

[6] M. De Angelis, S. Perno, and A. Reggio, "Dynamic response and optimal design of structures with large mass ratio TMD," *Earthquake Engineering & Structural Dynamics*, vol. 41, no. 1, pp. 41–60, 2012.

[7] M. C. Smith, "Synthesis of mechanical networks: the inerter," *IEEE Transactions on Automatic Control*, vol. 47, no. 10, pp. 1648–1662, 2002.

[8] I. F. Lazar, S. A. Neild, and D. J. Wagg, "Using an inerter-based device for structural vibration suppression," *Earthquake Engineering & Structural Dynamics*, vol. 43, no. 8, pp. 1129–1147, 2014.

[9] I. F. Lazar, S. A. Neild, and D. J. Wagg, "Vibration suppression of cables using tuned inerter dampers," *Engineering Structures*, vol. 122, pp. 62–71, 2016.

[10] L. Marian and A. Giaralis, "Optimal design of a novel tuned mass-damper-inerter (TMDI) passive vibration control configuration for stochastically support-excited structural systems," *Probabilistic Engineering Mechanics*, vol. 38, pp. 156–164, 2014.

[11] D. De Domenico and G. Ricciardi, "Improving the dynamic performance of base-isolated structures via tuned mass damper and inerter devices: a comparative study," *Structural Control and Health Monitoring*, vol. 25, no. 10, p. e2234, 2018.

[12] D. De Domenico, H. Qiao, Q. Wang, Z. Zhu, and G. Marano, "Optimal design and seismic performance of Multi-Tuned Mass Damper Inerter (MTMDI) applied to adjacent high-rise buildings," *The Structural Design of Tall and Special Buildings*, vol. 29, no. 14, Article ID e1781, 2020.

[13] L. Y. Cao, C. X. Li, and C. Xu, "Performance of multiple tuned mass dampers-inerters for structures under harmonic ground acceleration," *Smart Structures and Systems*, vol. 26, pp. 49–61, 2020.

[14] Q. Wang, N. D. Tiwari, H. Qiao, and Q. Wang, "Inerter-based tuned liquid column damper for seismic vibration control of a single-degree-of-freedom structure," *International Journal of Mechanical Sciences*, vol. 184, Article ID 105840, 2020.

[15] A. Di Matteo, C. Masnata, C. Adam, and A. Pirrotta, "Optimal design of tuned liquid column damper inerter for vibration control," *Mechanical Systems and Signal Processing*, vol. 167, Article ID 108553, 2022.

[16] L. Y. Cao and C. X. Li, "Tuned tandem mass dampers-inerters with broadband high effectiveness for structures under white noise base excitations," *Structural Control and Health Monitoring*, vol. 26, no. 4, Article ID e2319, 2019.

[17] C. X. Li, H. Pan, and L. Y. Cao, "Tuned tandem mass dampers-inerters for suppressing vortex-induced vibration of super-tall buildings," *Engineering Structures*, vol. 270, Article ID 114831, 2022.

[18] M. Fahimi Farzam and H. Hojat Jalali, "Tandem tuned mass damper inerter for passive control of buildings under seismic loads," *Structural Control and Health Monitoring*, vol. 29, no. 9, Article ID e2987, 2022.

[19] H. Hojat Jalali and M. Fahimi Farzam, "Inerter-connected double tuned mass damper for passive control of buildings under seismic excitation," *Periodica Polytechnica: Civil Engineering*, vol. 66, no. 2, pp. 421–432, 2022.

[20] H. Zhu, Y. Li, W. Shen, and S. Zhu, "Mechanical and energy-harvesting model for electromagnetic inertial mass dampers," *Mechanical Systems and Signal Processing*, vol. 120, pp. 203–220, 2019.

[21] J. Dai, Z. D. Xu, and P. P. Gai, "Tuned mass-damper-inerter control of wind-induced vibration of flexible structures based on inerter location," *Engineering Structures*, vol. 199, Article ID 109585, 2019.

[22] D. Pietrosanti, M. De Angelis, and M. Basili, "Optimal design and performance evaluation of systems with tuned mass damper inerter (TMDI)," *Earthquake Engineering & Structural Dynamics*, vol. 46, no. 8, pp. 1367–1388, 2017.

[23] A. Giaralis and F. Petrini, "Wind-induced vibration mitigation in tall buildings using the tuned mass-damper-inerter," *Journal of Structural Engineering*, vol. 143, no. 9, Article ID 4017127, 2017.

[24] Q. Wang, H. Qiao, W. Li, Y. You, Z. Fan, and N. Tiwari, "Parametric optimization of an inerter-based vibration absorber for wind-induced vibration mitigation of a tall building," *Wind and Structures*, vol. 31, no. 3, pp. 241–253, 2020.

[25] Q. Wang, H. Qiao, D. De Domenico, Z. Zhu, and Z. Xie, "Wind-induced response control of high-rise buildings using inerter-based vibration absorbers," *Applied Sciences*, vol. 9, no. 23, p. 5045, 2019.

[26] N. Su, Y. Xia, and S. T. Peng, "Filter-based inerter location dependence analysis approach of Tuned mass damper inerter (TMDI) and optimal design," *Engineering Structures*, vol. 250, Article ID 113459, 2022.

[27] A. Kaveh, M. Fahimi Farzam, and H. Hojat Jalali, "Statistical seismic performance assessment of tuned mass damper inerter," *Structural Control and Health Monitoring*, vol. 27, no. 10, Article ID e2602, 2020.

[28] A. Kaveh, M. Fahimi Farzam, H. Hojat Jalali, and R. Maroofiazar, "Robust optimum design of a tuned mass damper inerter," *Acta Mechanica*, vol. 231, no. 9, pp. 3871–3896, 2020.

[29] H. Qiao, P. Huang, D. De Domenico, and Q. Wang, "Targeted modal response control of structures with inerter-based vibration absorbers considering modal interaction effects," *Journal of Building Engineering*, vol. 64, Article ID 105692, 2023.

[30] G. Kerschen, J. J. Kowtko, D. M. McFarland, L. A. Bergman, and A. F. Vakakis, "Theoretical and experimental study of multimodal targeted energy transfer in a system of coupled oscillators," *Nonlinear Dynamics*, vol. 47, no. 1-3, pp. 285–309, 2006.

[31] B. Vaurigaud, A. Ture Savadkoohi, and C. H. Lamarque, "Targeted energy transfer with parallel nonlinear energy sinks. Part I: design theory and numerical results," *Nonlinear Dynamics*, vol. 66, no. 4, pp. 763–780, 2011.

[32] J. Wang, B. Wang, Z. Liu, C. Zhang, and H. Li, "Experimental and numerical studies of a novel asymmetric nonlinear mass damper for seismic response mitigation," *Structural Control and Health Monitoring*, vol. 27, no. 4, Article ID e2513, 2020.

[33] Y.-W. Zhang, Y.-N. Lu, W. Zhang et al., "Nonlinear energy sink with inerter," *Mechanical Systems and Signal Processing*, vol. 125, pp. 52–64, 2019.

[34] Z. Zhang, Z.-Q. Lu, H. Ding, and L.-Q. Chen, "An inertial nonlinear energy sink," *Journal of Sound and Vibration*, vol. 450, pp. 199–213, 2019.

[35] A. Javidialesaadi and N. E. Wierschem, "An inerter-enhanced nonlinear energy sink," *Mechanical Systems and Signal Processing*, vol. 129, pp. 449–454, 2019.

[36] J. J. Wang, B. Wang, C. Zhang, and Z. B. Liu, "Effectiveness and robustness of an asymmetric nonlinear energy sink-inerter for dynamic response mitigation," *Earthquake Engineering & Structural Dynamics*, vol. 50, no. 6, pp. 1628–1650, 2021.

[37] J. J. Wang, C. Zhang, and Y. Q. Zheng, "An inerter-enhanced asymmetric nonlinear energy sink for response mitigation of structures subjected to harmonic and seismic ground excitations," *Structural Control and Health Monitoring*, vol. 29, no. 12, Article ID e3104, 2022.

[38] S. Elias and V. Matsagar, "Wind response control of tall buildings with a tuned mass damper," *Journal of Building Engineering*, vol. 15, pp. 51–60, 2018.

[39] E. Simiu and R. H. Scanlan, *Wind Effects on Structures: An Introduction to Wind Engineering*, Wiley, New York, NY, USA, 1986.

[40] A. G. Davenport, "Note on the distribution of the largest value of a random function with application to gust loading," *Proceedings- Institution of Civil Engineers*, vol. 28, no. 2, pp. 187–196, 1964.

[41] Ministry of Housing and Urban-Rural Development of the People's Republic of China, "Load code for the design of building structures," China Architecture & Building Press, Beijing, China, GB50009-2012, 2012.

[42] J. D. Holmes, *Wind Loading of Structures*, Taylor & Francis Group, London, UK, 1 edition, 2001.

[43] S. Elias and V. Matsagar, "Research developments in vibration control of structures using passive tuned mass dampers," *Annual Reviews in Control*, vol. 44, pp. 129–156, 2017.

[44] X. Lu, Q. Zhang, D. Weng et al., "Improving performance of a super tall building using a new eddy-current tuned mass damper," *Structural Control and Health Monitoring*, vol. 24, no. 3, Article ID e1882, 2017.

[45] K. Deb, A. Pratap, S. Agarwal, and T. Meyarivan, "A fast and elitist multiobjective genetic algorithm: nsga-II," *IEEE Transactions on Evolutionary Computation*, vol. 6, no. 2, pp. 182–197, 2002.

[46] M. M. Selwanis, G. R. Franzini, C. Béguin, and F. P. Gosselin, "Multi-ball rotative nonlinear energy sink for galloping mitigation," *Journal of Sound and Vibration*, vol. 526, Article ID 116744, 2022.

[47] M. Oliva, G. Barone, F. Lo Iacono, and G. Navarra, "Nonlinear energy sink and Eurocode 8: an optimal design approach based on elastic response spectra," *Engineering Structures*, vol. 221, Article ID 111020, 2020.

[48] H. Qiao, P. Huang, D. De Domenico, and Q. Wang, "Structural control of high-rise buildings subjected to multi-hazard excitations using inerter-based vibration absorbers," *Engineering Structures*, vol. 266, Article ID 114666, 2022.

[49] R. Ruiz, A. A. Taflanidis, D. Lopez-Garcia, and C. R. Vetter, "Life-cycle based design of mass dampers for the Chilean region and its application for the evaluation of the effectiveness of tuned liquid dampers with floating roof," *Bulletin of Earthquake Engineering*, vol. 14, no. 3, pp. 943–970, 2016.

[50] I. Gidaris and A. A. Taflanidis, "Performance assessment and optimization of fluid viscous dampers through life-cycle cost criteria and comparison to alternative design approaches," *Bulletin of Earthquake Engineering*, vol. 13, no. 4, pp. 1003–1028, 2015.

[51] R. Ruiz, A. Taflanidis, A. Giaralis, D. Lopez-Garcia, and D. Lopez-Garcia, "Risk-informed optimization of the tuned mass-damper-inerter (TMDI) for the seismic protection of multi-storey building structures," *Engineering Structures*, vol. 177, pp. 836–850, 2018.